LETTER

doi:10.1038/nature13032

A large source of low-volatility secondary organic aerosol

Mikael Ehn[1,2], Joel A. Thornton[2,3], Einhard Kleist[4], Mikko Sipilä[2], Heikki Junninen[2], Iida Pullinen[1], Monika Springer[1], Florian Rubach[1], Ralf Tillmann[1], Ben Lee[3], Felipe Lopez-Hilfiker[3], Stefanie Andres[1], Ismail-Hakki Acir[1], Matti Rissanen[2], Tuija Jokinen[2,5], Siegfried Schobesberger[2], Juha Kangasluoma[2], Jenni Kontkanen[2], Tuomo Nieminen[2,6], Theo Kurtén[7], Lasse B. Nielsen[8], Solvejg Jørgensen[8], Henrik G. Kjaergaard[8], Manjula Canagaratna[9], Miikka Dal Maso[10], Torsten Berndt[5], Tuukka Petäjä[2], Andreas Wahner[1], Veli-Matti Kerminen[2], Markku Kulmala[2], Douglas R. Worsnop[2,9], Jürgen Wildt[4] & Thomas F. Mentel[1]

Forests emit large quantities of volatile organic compounds (VOCs) to the atmosphere. Their condensable oxidation products can form secondary organic aerosol, a significant and ubiquitous component of atmospheric aerosol[1,2], which is known to affect the Earth's radiation balance by scattering solar radiation and by acting as cloud condensation nuclei[3]. The quantitative assessment of such climate effects remains hampered by a number of factors, including an incomplete understanding of how biogenic VOCs contribute to the formation of atmospheric secondary organic aerosol. The growth of newly formed particles from sizes of less than three nanometres up to the sizes of cloud condensation nuclei (about one hundred nanometres) in many continental ecosystems requires abundant, essentially non-volatile organic vapours[4–6], but the sources and compositions of such vapours remain unknown. Here we investigate the oxidation of VOCs, in particular the terpene α-pinene, under atmospherically relevant conditions in chamber experiments. We find that a direct pathway leads from several biogenic VOCs, such as monoterpenes, to the formation of large amounts of extremely low-volatility vapours. These vapours form at significant mass yield in the gas phase and condense irreversibly onto aerosol surfaces to produce secondary organic aerosol, helping to explain the discrepancy between the observed atmospheric burden of secondary organic aerosol and that reported by many model studies[2]. We further demonstrate how these low-volatility vapours can enhance, or even dominate, the formation and growth of aerosol particles over forested regions, providing a missing link between biogenic VOCs and their conversion to aerosol particles. Our findings could help to improve assessments of biosphere–aerosol–climate feedback mechanisms[6–8], and the air quality and climate effects of biogenic emissions generally.

We studied the oxidation of several monoterpenes and other VOCs under atmospherically relevant conditions in the highly instrumented Jülich Plant Atmosphere Chamber, JPAC[9], a continuously stirred tank reactor (see Methods for experimental details). We focus here on α-pinene, as it alone constitutes nearly 50% of global monoterpene emissions[10]. Using a high-resolution chemical ionization mass spectrometer, CI-APi-TOF[11] (see Methods) we detected highly oxygenated, high-molecular-mass gas-phase oxidation products from several precursors following both ozonolysis and reaction with the hydroxyl radical (OH). Figure 1 depicts an α-pinene ozonolysis spectrum displaying monomer ($C_{10}H_{14-16}O_{7-11}$) and dimer ($C_{19-20}H_{28-32}O_{10-18}$) patterns. We collectively refer to such products, both monomers and dimers, as extremely low-volatility organic compounds (ELVOCs[12]). We estimate an uncertainty of ±50% for absolute concentrations of ELVOCs (see Methods) whereas relative changes are precise to <10%. Importantly, with the experimental conditions probed in JPAC, we could closely replicate both daytime and nighttime ELVOC mass spectra recorded at a boreal forest site in Hyytiälä, Finland (Extended Data Fig. 1a, b).

During steady-state α-pinene ozonolysis experiments, the total ELVOC concentration had a near-linear dependence on the amount of α-pinene reacting with O_3 (Fig. 2a), indicative of first-generation products. The majority of the data are explained by ELVOC molar yields of 6–8%. Owing to the large molecular masses of the ELVOCs, a 6% molar yield translates to a mass yield of 14% (see Methods). On the basis of structure–activity relationships[13], ELVOCs have vapour pressures orders of magnitude lower than most previously identified gas-phase oxidation products of VOCs, and should thus condense irreversibly to form a substantial component of α-pinene secondary organic aerosol (SOA)[10,14]. Consistent with this idea, the addition of 100-nm solid ammonium sulphate particles to the chamber under constant α-pinene ozonolysis conditions caused both a clear decrease in ELVOC concentration (quantitatively explained by diffusion-limited condensation to the ammonium sulphate particles) and a corresponding increase in SOA (Fig. 2b). Gas-phase concentrations of abundant semi-volatile organic compounds (SVOCs) such as pinic and pinonic acid were not observed to decrease appreciably when seed aerosol was added (Extended Data Fig. 2b).

At low total aerosol loadings, the measured SOA mass in our experiments was almost entirely explained by ELVOCs lost via condensation to the ammonium sulphate particles (Fig. 2c). Even at higher SOA loadings (~10 μg m^{-3}), at which SVOCs probably begin contributing more via absorptive partitioning[15], roughly two-thirds of the SOA mass was still explained by ELVOC condensation. Additionally, the formed SOA and the condensed ELVOCs had essentially the same O/C and H/C elemental ratios of 0.7 ± 0.1 and 1.5 ± 0.1, respectively (Extended Data Fig. 3). This further supports ELVOCs being the main SOA source at low loadings, and to our knowledge, we provide the first demonstration of mass closure between condensation of gas-phase oxidation products and SOA mass formed during monoterpene oxidation.

Although it is perhaps surprising that a previously unmeasured class of gas-phase oxidation products can dominate α-pinene ozonolysis SOA at low loadings, irreversible ELVOC condensation helps explain seemingly disparate characteristics of α-pinene SOA. Relatively high SOA mass yields have been found[16] at low loadings, which suggests the presence of a very low-volatility product. Additionally, several independent methods suggest that α-pinene SOA formed at low loadings is semi-solid with slow evaporation, consistent with the presence of a very low-volatility, highly oxygenated, high-molecular-mass component[14,17,18]. These characteristics have called into question the use of equilibrium absorptive partitioning theory to describe α-pinene SOA[18]. Our results

[1]Institute for Energy and Climate Research (IEK-8), Forschungszentrum Jülich, 52425 Jülich, Germany. [2]Department of Physics, PO Box 64, 00014 University of Helsinki, Finland. [3]Department of Atmospheric Sciences, University of Washington, Seattle, Washington 98195, USA. [4]Institute of Bio- and Geosciences (IBG-2), Forschungszentrum Jülich, 52425 Jülich, Germany. [5]Institute for Tropospheric Research (TROPOS), 04318 Leipzig, Germany. [6]Helsinki Institute of Physics, PO Box 64, 00014 University of Helsinki, Finland. [7]Department of Chemistry, PO Box 55, 00014 University of Helsinki, Finland. [8]Department of Chemistry, University of Copenhagen, Universitetsparken 5, 2100 Copenhagen Ø, Denmark. [9]Aerodyne Research, Inc., 45 Manning Road, Billerica, Massachusetts 01821, USA. [10]Department of Physics, Tampere University of Technology, PO Box 692, 33101 Tampere, Finland.

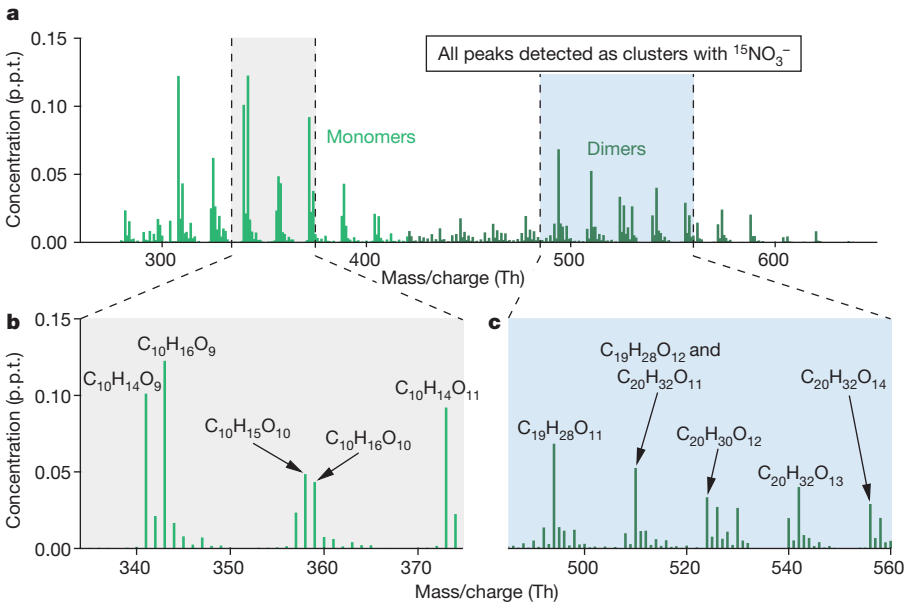

Figure 1 | Mass spectrum of ELVOCs produced by α-pinene ozonolysis. The spectral fingerprint (**a**) displays clear 'monomer' ($C_{10}H_{14-16}O_{7-11}$, example peaks in **b**) and 'dimer' ($C_{19-20}H_{28-32}O_{10-18}$, example peaks in **c**) distributions. Such compounds have been previously identified, but never quantified, in naturally charged ions[30]. The detection of ELVOCs in the CI-APi-TOF, used in the measurements reported here, relies on their efficient clustering with isotopically labelled nitrate reagent ions. Only a few other α-pinene ozonolysis products are detected outside the plotted range, owing to the selectivity of nitrate clustering in the CI-APi-TOF. Mass/charge ratio is plotted in units of thomsons (Th), which equal daltons (Da) per elementary charge (*e*). p.p.t., parts per trillion.

do not contradict absorptive partitioning theory. Rather, our findings will significantly improve its predictive capability by quantifying the formation of extremely low vapour pressure compounds into which SVOCs can presumably partition or react as loadings increase.

In light of the importance of ELVOCs illustrated above, we performed additional experiments and kinetic model calculations aimed at understanding their chemical properties and formation mechanisms. Our detailed findings (Methods) are consistent with a pathway mainly driven by organic peroxy radical (RO_2) chemistry, supported in part by our ability to directly detect certain highly oxygenated RO_2, and the response of these radicals and ELVOCs to nitric oxide (NO) additions. We hypothesize, backed by experiments using isotopically labelled reactants, that a fraction of RO_2 formed from ozonolysis achieve a high oxygen content by rapid molecular oxygen (O_2) additions following intramolecular hydrogen abstractions. This process has only recently been proposed to occur under atmospheric conditions[19,20], and the successive H-abstractions/O_2-additions have typically been assumed to terminate before molecules could reach the high O/C ratios we observe. Ozonolysis of endocyclic alkenes (such as α-pinene) appears to be especially efficient at producing ELVOCs, probably because this reaction forms products where subsequent H-abstractions are favoured, though significant amounts were also produced from OH-oxidation of

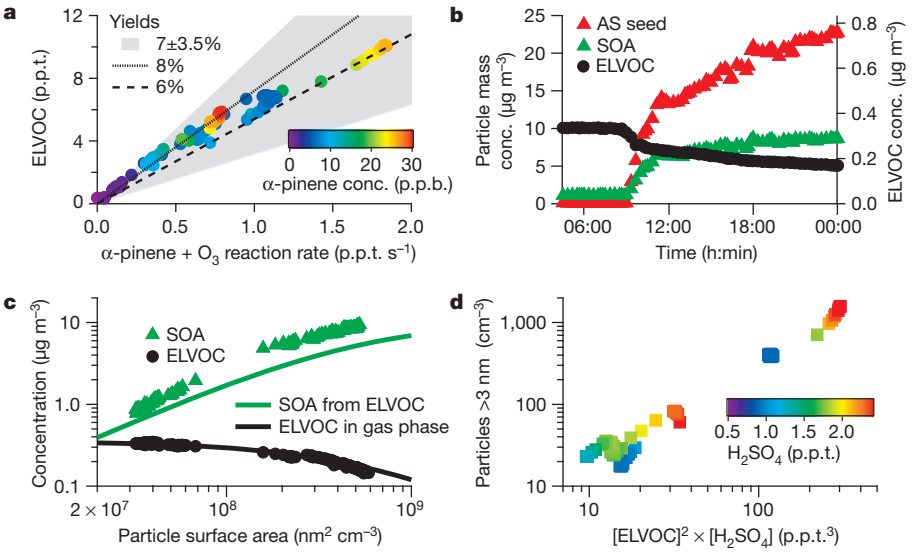

Figure 2 | ELVOC chamber experiments. **a**, Measured total ELVOCs plotted against α-pinene ozonolysis rate. Points are coloured by α-pinene concentration, showing that ELVOC concentrations only depend on the product of [O_3] and [α-pinene]. The lines correspond to ELVOC molar yields (see key) from α-pinene ozonolysis, the shaded area denotes a 50% uncertainty. The hydroxyl radical makes a minor contribution to ELVOCs under these conditions (Extended Data Fig. 2a). **b**, Ammonium sulphate (AS) seed addition (red triangles, left axis) causes a decrease in ELVOCs (black dots, right axis) due to an increased particulate condensation sink, and a corresponding increase in SOA mass (green triangles, left axis) is detected. **c**, The dependence of ELVOC and SOA concentrations on particle surface area (condensation sink). Measured data points (symbols) correspond to those in **b**. The lines depict the theoretically expected behaviour (see Methods) of ELVOCs (black line) and the corresponding accumulated SOA mass from ELVOC condensation (green line). The different chamber lifetimes ($t_{SOA} \approx 45$ min, $t_{ELVOC} < 1.5$ min) cause the enhancement of SOA mass compared to condensed ELVOC mass (see Methods). **d**, The concentration of particles larger than 3 nm is strongly dependent on both H_2SO_4 and ELVOC concentrations, with [ELVOC]^2·[H_2SO_4] producing a near-linear slope.

most VOCs. Based on insights from the above experiments, ELVOCs are likely to contain multiple hydroperoxide moieties, in accordance with their high O/C and H/C ratios. The competition between sequential H-abstractions and termination reactions with other RO_2 and NO in high-loading or high-NO_x experiments, respectively, will potentially change the chemical nature of the SOA by reducing ELVOC formation in favour of less oxidized compounds.

ELVOCs have probably been a major SOA source in most previous chamber experiments conducted at atmospherically relevant α-pinene loadings, though only the recent application of the CI-APi-TOF has facilitated the detection of gas-phase ELVOCs, individually present at sub-parts-per-trillion mixing ratios. This capability allowed us to determine the ELVOC yield, and by adding inorganic seed particles, convert more of this potential SOA into actual SOA mass. In our experiments, the apparent SOA mass yield increased from ~1% with no seed particles to ~10% at the highest seed particle concentrations, which were still not high enough to fully overcome ELVOC losses to walls (see Methods). With much higher amounts of reacted α-pinene than in our experiments, equilibrium partitioning[15] and reactive uptake[21] of SVOCs become more important sources of SOA mass, thus masking the specific contribution of ELVOCs, though in most cases ELVOCs still probably provide an initial organic medium required for such processes. Although outside the scope of this study, once in the condensed phase, molecules with multiple hydroperoxide moieties will probably participate in accretion reactions[2,21], further decreasing the volatility of the reactants. Such reactions, and possible thermal decomposition on heating[22], make it challenging, if not impossible, to detect the same ELVOCs that had condensed from the gas-phase by analysing the SOA[2]. Future efforts should focus on determining the exact structures of gas-phase ELVOCs, and the atmospheric evolution of the SOA formed through ELVOC condensation.

The finding of irreversibly condensing α-pinene ozonolysis products formed at 14–19% mass yield at the low reactant concentrations in our chamber (Fig. 2a) has significant consequences for the SOA yield estimated from this reaction in the atmosphere. Our results suggest ELVOCs alone can drive the SOA mass yield from α-pinene ozonolysis beyond 10% above the forest canopy where the condensational sink is the dominant loss for low-volatility vapours. However, existing α-pinene ozonolysis parameterizations[2] predict that less than 5% of the products have vapour pressures below 1 μg m^{-3}. Applying such yield parameterizations to the atmosphere would thus underestimate SOA, a feature common to current models[2]. Other ELVOC losses (for example, deposition, photolysis or OH oxidation) and shifts in the monomer to dimer ratio (see Methods) may somewhat lower the SOA mass formation potential of ELVOCs, but their contribution to α-pinene ozonolysis SOA will almost certainly remain important, as we further illustrate below.

As ELVOCs form at significant mass yield and condense irreversibly onto surfaces, they should also contribute to the growth of newly formed particles. We found that concentrations of particles larger than ~3 nm in our chamber depend on both sulphuric acid vapour (H_2SO_4) and ELVOC concentrations, scaling approximately linearly with $[ELVOC]^2 \times [H_2SO_4]$ (Fig. 2d, Extended Data Fig. 4f–i). Thus, although H_2SO_4 is important in the initial formation of growing clusters smaller than a few nanometres, as earlier studies have shown[4,23], the formation rate of 3-nm particles is already more strongly driven by ELVOCs under these experimental conditions (see Extended Data Fig. 6d). We therefore propose that the ELVOCs we detect from monoterpene oxidation help explain the appearance and subsequent rapid growth of new particles observed in forested regions[4,5]. Indeed, we find that ELVOC dimers are large enough to act as nano-condensation nuclei[24] (Extended Data Fig. 4a–e). Importantly, using recent direct measurements of ELVOCs during new particle formation and growth events in the Hyytiälä forest, we show that ELVOCs are abundant enough to explain the observed particle growth rates in the 5–50 nm range (Fig. 3).

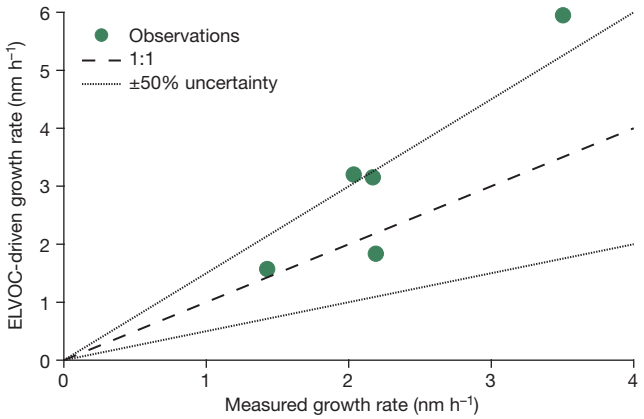

Figure 3 | Comparison of measured particle growth rates with those predicted from measured ELVOC concentrations in Hyytiälä forest. Measured growth rates are over the range 5–50 nm; details are given in Methods. The dashed line shows the 1:1 ratio, and the dotted lines correspond to 0.5:1 and 1:1.5, that is, a 50% uncertainty. The ELVOC concentrations are clearly in the right concentration range to be able to explain the majority of the growth of newly formed particles in the boreal forest. We thus have detected and quantified the nearly non-volatile organic compounds required to explain atmospheric particle growth rates, as predicted by previous studies[4,5].

We have provided the first molecular elucidation and quantification of a direct and ubiquitous source of ELVOCs produced in the gas phase from oxidation of monoterpenes and other VOCs. This source is capable of explaining nanoparticle growth in boreal regions and a significant fraction of low-volatility SOA currently missing, or poorly described, in atmospheric models[1,2,4,5]. A schematic illustration of the atmospheric roles of ELVOCs is presented in Fig. 4. Some atmospheric models can replicate monoterpene SOA by assuming irreversible condensation of unspecified first-generation oxidation products[25], an approach now validated and clarified by our results. We have also demonstrated mechanisms whereby anthropogenic emissions (SO_2, NO) can affect the contribution of biogenic VOCs to aerosol particle formation and growth

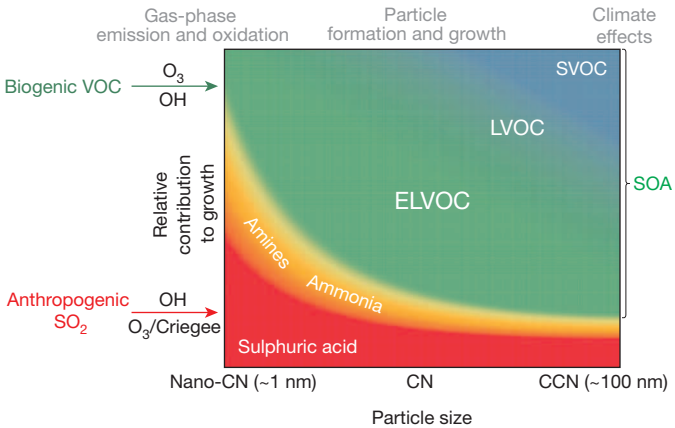

Figure 4 | The importance of precursor vapours for aerosol growth at different sizes. This schematic overview depicts the path from emissions of volatile compounds, via aerosol particles, to their climate effects (grey labels at top). Our findings suggest that ELVOCs are major contributors to condensational growth at all sizes, ranging from newly formed particles (nano-condensation nuclei, nano-CN) through to cloud condensation nuclei (CCN). The relative roles of different vapours, described by corresponding colours (H_2SO_4, red; bases, orange; organics, varying shades of green), will vary depending on location and prevailing meteorological conditions, but this figure provides an estimate of the average contribution of the most important precursor vapours to particle growth in boreal forest-type environments. Both biogenic VOCs (green arrow on vertical axis) and anthropogenic SO_2 emissions (red arrow on vertical axis) can enhance the formation and growth of particles to climate-relevant sizes.

by interacting with ELVOCs directly (for example, H_2SO_4) or altering their formation pathways (for example, NO, see Methods).

Our results clearly demonstrate that current oxidation mechanisms underestimate the role of ozone and RO_2 isomerization chemistry in producing highly oxygenated low-volatility compounds. This underlines the importance of accurately predicting oxidant levels and biogenic VOC emissions. Past or future changes in the ozone/OH ratio[26,27] may represent an additional anthropogenic influence on climate via ELVOC formation and thus concentrations of SOA and cloud condensation nuclei. Moreover, regional and global climate change influences VOC emissions by terrestrial vegetation[28,29]. Our new insights into ELVOC formation may help to more accurately quantify the effects of changes in biogenic VOC emissions—specifically, the effects on new particle formation, abundance of cloud condensation nuclei, and possible related climate feedbacks[6–8].

METHODS SUMMARY

The majority of the presented measurements were performed at the Jülich Plant Atmosphere Chamber facility (JPAC[9]). Contrary to many other chamber studies where a batch of VOCs is oxidized over a certain period of time, the JPAC measurements were mainly carried out in a continuously stirred tank reactor under steady-state conditions. This means that a constant flow of reactants and oxidants were added to the chamber until the chamber air (including VOCs, ELVOCs and particles) reached steady-state. The average residence time in the chamber was ~45 min. All ambient data presented in this work were measured at the Station for Measuring Ecosystem-Atmosphere Relations (SMEAR II) in Hyytiälä, Southern Finland.

The efficient ELVOC detection was made possible by the use of nitrate ion clustering at atmospheric pressure, using the CI-APi-TOF[11]. This instrument is optimal for ELVOC detection, as its high sample flow rate and nearly wall-less inlet design minimizes losses of low-volatility vapours. The mass spectrometer has a high throughput of sampled ions, and high mass resolution allowing elemental composition determination up to masses where ELVOCs are detected (Fig. 1). Additionally, the selectivity of nitrate chemical ionization keeps the spectrum clean from many background contaminants, as well as more abundant, less oxidized compounds.

Online Content Any additional Methods, Extended Data display items and Source Data are available in the online version of the paper; references unique to these sections appear only in the online paper.

Received 7 August 2013; accepted 14 January 2014.

1. Jimenez, J. L. *et al.* Evolution of organic aerosols in the atmosphere. *Science* **326,** 1525–1529 (2009).
2. Hallquist, M. *et al.* The formation, properties and impact of secondary organic aerosol: current and emerging issues. *Atmos. Chem. Phys.* **9,** 5155–5236 (2009).
3. Solomon, S. *et al.* (eds) *Climate Change 2007: The Physical Science Basis* (Cambridge Univ. Press, 2007).
4. Kulmala, M. *et al.* Direct observations of atmospheric aerosol nucleation. *Science* **339,** 943–946 (2013).
5. Riipinen, I. *et al.* Organic condensation: a vital link connecting aerosol formation to cloud condensation nuclei (CCN) concentrations. *Atmos. Chem. Phys.* **11,** 3865–3878 (2011).
6. Paasonen, P. *et al.* Warming-induced increase in aerosol number concentration likely to moderate climate change. *Nature Geosci.* **6,** 438–442 (2013).
7. Carslaw, K. S. *et al.* A review of natural aerosol interactions and feedbacks within the Earth system. *Atmos. Chem. Phys.* **10,** 1701–1737 (2010).
8. Spracklen, D. V., Bonn, B. & Carslaw, K. S. Boreal forests, aerosols and the impacts on clouds and climate. *Phil. Trans. R. Soc. A* **366,** 4613–4626 (2008).
9. Mentel, T. F. *et al.* Photochemical production of aerosols from real plant emissions. *Atmos. Chem. Phys.* **9,** 4387–4406 (2009).
10. Pathak, R. K., Stanier, C. O., Donahue, N. M. & Pandis, S. N. Ozonolysis of α-pinene at atmospherically relevant concentrations: temperature dependence of aerosol mass fractions (yields). *J. Geophys. Res. D* **112,** D03201 (2007).
11. Jokinen, T. *et al.* Atmospheric sulphuric acid and neutral cluster measurements using CI-APi-TOF. *Atmos. Chem. Phys.* **12,** 4117–4125 (2012).
12. Donahue, N. M., Kroll, J. H., Pandis, S. N. & Robinson, A. L. A two-dimensional volatility basis set – Part 2: diagnostics of organic-aerosol evolution. *Atmos. Chem. Phys.* **12,** 615–634 (2012).
13. Capouet, M. & Muller, J. F. A group contribution method for estimating the vapour pressures of α-pinene oxidation products. *Atmos. Chem. Phys.* **6,** 1455–1467 (2006).
14. Grieshop, A. P., Donahue, N. M. & Robinson, A. L. Is the gas-particle partitioning in α-pinene secondary organic aerosol reversible? *Geophys. Res. Lett.* **34,** L14810 (2007).
15. Pankow, J. F. Gas/particle partitioning of neutral and ionizing compounds to single and multiple-phase aerosol particles. 1. Unified modeling framework. *Atmos. Environ.* **37,** 3323–3333 (2003).
16. Shilling, J. E. *et al.* Particle mass yield in secondary organic aerosol formed by the dark ozonolysis of α-pinene. *Atmos. Chem. Phys.* **8,** 2073–2088 (2008).
17. Virtanen, A. *et al.* An amorphous solid state of biogenic secondary organic aerosol particles. *Nature* **467,** 824–827 (2010).
18. Vaden, T. D., Imre, D., Beránek, J., Shrivastava, M. & Zelenyuk, A. Evaporation kinetics and phase of laboratory and ambient secondary organic aerosol. *Proc. Natl Acad. Sci. USA* **108,** 2190–2195 (2011).
19. Vereecken, L., Muller, J. F. & Peeters, J. Low-volatility poly-oxygenates in the OH-initiated atmospheric oxidation of α-pinene: impact of non-traditional peroxyl radical chemistry. *Phys. Chem. Chem. Phys.* **9,** 5241–5248 (2007).
20. Crounse, J. D., Nielsen, L. B., Jørgensen, S., Kjaergaard, H. G. & Wennberg, P. O. Autoxidation of organic compounds in the atmosphere. *J. Phys. Chem. Lett.* 3513–3520 (2013).
21. Shiraiwa, M. *et al.* Size distribution dynamics reveal particle-phase chemistry in organic aerosol formation. *Proc. Natl Acad. Sci. USA* **110,** 11746–11750 (2013).
22. Hall, W. A. & Johnston, M. V. The thermal-stability of oligomers in alpha-pinene secondary organic aerosol. *Aerosol Sci. Technol.* **46,** 983–989 (2012).
23. Sipilä, M. *et al.* The role of sulfuric acid in atmospheric nucleation. *Science* **327,** 1243–1246 (2010).
24. McMurry, P. H., Kulmala, M. & Worsnop, D. R. Special issue on aerosol measurements in the 1 nm range. *Aerosol Sci. Technol.* **45,** i (2011).
25. Spracklen, D. V. *et al.* Aerosol mass spectrometer constraint on the global secondary organic aerosol budget. *Atmos. Chem. Phys.* **11,** 12109–12136 (2011).
26. Naik, V. *et al.* Preindustrial to present-day changes in tropospheric hydroxyl radical and methane lifetime from the Atmospheric Chemistry and Climate Model Intercomparison Project (ACCMIP). *Atmos. Chem. Phys.* **13,** 5277–5298 (2013).
27. Parrish, D. D. *et al.* Long-term changes in lower tropospheric baseline ozone concentrations at northern mid-latitudes. *Atmos. Chem. Phys.* **12,** 11485–11504 (2012).
28. Guenther, A. *et al.* A model of natural volatile organic compound emissions. *J. Geophys. Res.* **100,** 8873–8892 (1995).
29. Young, P. J., Arneth, A., Schurgers, G., Zeng, G. & Pyle, J. A. The CO_2 inhibition of terrestrial isoprene emission significantly affects future ozone projections. *Atmos. Chem. Phys.* **9,** 2793–2803 (2009).
30. Ehn, M. *et al.* Gas phase formation of extremely oxidized pinene reaction products in chamber and ambient air. *Atmos. Chem. Phys.* **12,** 5113–5127 (2012).

Acknowledgements M.E. was supported by the Emil Aaltonen foundation; J.A.T. was supported by the US Department of Energy, Office of Science (DE-SC0006867). This work was supported by the ERC Advanced Grant EU-FP7-ATMNUCLE (project no. 227463), the EU-FP7 project PEGASOS (project no. 265148), the Academy of Finland (project no. 251427 and 266388) and by the Academy of Finland Center of Excellence programme (project no. 1118615). We thank M. Kajos, S. Schallhart and T. Ruuskanen for measurement support, O. Kupiainen for collision rate calculations, and the tofTools team for analysis tools for mass spectra.

Author Contributions M.E., J.A.T., E.K., I.P., M. Springer, F.R., R.T., B.L., F.L.-H., S.A., I.-H.A., M.R., T.J., J. Kangasluoma, T.B. and J.W. conducted the data collection and analysis. H.J. and M.C. provided data analysis tools. J. Kontkanen and T.N. analysed the ambient data. M.E., J.A.T., T.K., L.B.N., S.J., H.G.K. and T.F.M. provided model calculations and developed the formation mechanism. M.E. and J.A.T. wrote the manuscript. M. Sipilä, M.D.M., T.P., A.W., V.-M.K., M.K., D.W. and T.F.M. did data interpretation and editing of the manuscript. All authors discussed the results and commented on the paper.

Author Information Reprints and permissions information is available at www.nature.com/reprints. The authors declare no competing financial interests. Readers are welcome to comment on the online version of the paper. Correspondence and requests for materials should be addressed to M.E. (mikael.ehn@helsinki.fi).

METHODS

Facilities and measurement sites. The majority of the presented results were measured in the Jülich Plant Atmosphere Chamber facility (JPAC), which consists of three glass chambers. As only one of these was used in this study, JPAC refers to this one chamber. The facility is described in detail elsewhere[9], and only the most important features are mentioned here.

The chamber is a 1,450-litre borosilicate glass chamber, operated as a continuously stirred flow reactor with an average residence time of 45 min (flow ~33 l min^{-1}). The chamber is mounted in a climate-controlled housing, and the temperature was kept constant at 16 ± 1 °C during the experiments. Relative humidity was controlled to 63 ± 3%. The chamber flow consisted of purified air, and variable amounts of ozone, different VOCs, NO_x, SO_2 and CO. Seed particles could be added as needed. Discharge lamps (HQI 400 W/D; Osram) were used to simulate the solar light spectrum in the reaction chamber. Infrared radiation (750–1,050 nm) was reflected by filters (type IR3; Prinz Optics) placed between the lamps and the chamber. The chamber also has two sets of ultraviolet lamps, one for photolysing ozone to produce OH (1 TUV lamp, Philips, TUV 40 W, λ_{max} = 254 nm), and a second for photolysing NO_2 to NO (12 discharge lamps Phillips TL 60 W/10-R; 60W, λ_{max} = 365 nm). The ultraviolet lamp used for OH production could be shielded to limit the amount of light entering the chamber, and thereby varying the OH production rate. Details of α-pinene, ozone and other varied parameters during experiments presented in Figs 1 and 2 are listed in Extended Data Fig. 6d. Throughout the Methods section, such details are listed in conjunction to the specific experiments. Reported OH concentrations were estimated from the difference in α-pinene flows entering and exiting the chamber, that is, the total amount of α-pinene reacted, after accounting for ozone reactions.

The chamber is surrounded by a suite of instrumentation measuring both the gas phase and particles. The most relevant instruments for this work are listed in the Instrumentation section below, and in addition, instruments to measure the following were deployed: ozone (Ansyco, ozone analyser, O3 41M), relative humidity (dew point mirror TP-2, Walz), total particle number >3 nm (Ultrafine Condensation Particle Counter, UCPC, 3025A, TSI), and the aerosol size distribution (15–600 nm, SMPS, TSI3081+TSI3786).

In addition to α-pinene, the ozonolysis of other biogenic and model alkene compounds was studied in JPAC. Extended Data Fig. 5a shows structures of the main compounds studied, which include other common monoterpenes, such as β-pinene and limonene, as well as smaller cyclic and acyclic alkenes. A subset of these compounds was also studied in the University of Helsinki and Institute for Tropospheric Research (Leipzig) flow reactors.

Cyclohexene and deuterated cyclohexene (isotope enrichment: 98%) ozonolysis was investigated at the University of Helsinki (UHEL) flow tube reactor (4.7 cm i.d., 205 cm). Experiments were performed at room temperature (T = 293 ± 3 K), relative humidity <1%, and ambient pressure using cryogenic nitrogen (N_2) or bottled synthetic air (N_2 and O_2) as carrier gas. Ozone was produced by a Dasibi 1008-PC ozone generator. The gas flow in the flow tube was 11 l min^{-1}, resulting in a residence time of ~20 s.

Reactions of α-pinene with 'normal' ozone ($^{16}O_3$) and isotopically labelled ozone ($^{18}O_3$, isotopic enrichment: 96%) were carried out in the Institute for Tropospheric Research — Laminar Flow Tube, IfT-LFT (i.d. 8 cm, length 505 cm) in Leipzig, Germany, at atmospheric pressure and relative humidity = 25% using purified synthetic air as the carrier gas[31]. A thermo-jacket maintained the tube at the adjusted temperature (293 ± 0.5 K). The humidified main carrier-gas stream was introduced at the top of the flow tube containing α-pinene. 55 cm downstream, $^{16}O_3$ or $^{18}O_3$ diluted in the carrier gas was added through an inlet. The design of the inlet nozzle ensured rapid gas mixing. $^{16}O_3$ and $^{18}O_3$ was supplied from an ozone generator UVP OG-2 using either $^{16}O_2$ or $^{18}O_2$ as the feed. The alkene concentration was measured by PTR-MS. ELVOC formation was measured using a CI-APi-TOF sampling the centre flow at the flow tube outlet.

All ambient data presented in this work were measured at the Station for Measuring Ecosystem-Atmosphere Relations (SMEAR II) in Hyytiälä, Southern Finland, and is taken to be representative of the boreal forest region that covers 8% of Earth's surface[32].

Instrumentation. The CI-APi-TOF[11] consists of a chemical ionization (CI) source[33] coupled to an atmospheric pressure interface time-of-flight mass spectrometer (APi-TOF)[34]. The reagent used in this study was nitric acid (HNO_3), and the charging of the sample took place by collisions with nitrate ion clusters $(HNO_3)_x(NO_3^-)$, x = 0–2. Some strong gas phase acids like sulphuric and malonic acid were directly ionized and detected as single, de-protonated ions, or in clusters with (HNO_3). However, most species were detected as adducts with NO_3^-, and to a lesser extent with $(HNO_3)(NO_3^-)$. In the JPAC experiments, isotopically labelled nitric acid ($H^{15}NO_3$) was used as reagent. This allowed us to distinguish between ^{15}N from the reagent and ^{14}N that has been incorporated into the sample molecules, for example, through reactions with ^{14}NO.

The design of the CI inlet is optimized for minimal wall contact of the sample. The sample flow rate is high (10 l min^{-1}), and the charging region (residence time ~200 ms) consists of two concentric flows, where the sample stays in the centre, surrounded by clean sheath air (20 l min^{-1}) containing the nitrate ions that are electrostatically pushed into the sample flow. Once the ions are sampled into the APi-TOF, they are guided through two differentially pumped chambers using segmented quadrupole mass filters. Collisions between ions and gas molecules will take place, but the energies are tuned low enough that only weakly bound clusters (for example, water clusters) will fragment. This is confirmed in earlier natural ion measurements using the APi-TOF, where the majority of signals are found in clusters[30,34,35].

To monitor a larger suite of oxygenated products from monoterpene oxidation, the University of Washington (UW) high resolution time of flight chemical ionization mass spectrometer (UW HR-ToF-CIMS) was deployed at JPAC using one of two different ionization schemes. Iodide adduct ionization and negative ion proton transfer ionization using acetate ions were used essentially as described previously[36–38]. See Extended Data Fig. 2b for example data. Aerosol particles were also collected onto a filter and, following temperature programmed thermal desorption, the volatilized vapours were sampled with the HR-ToF-CIMS.

VOCs and their oxidation products were measured by a proton transfer reaction mass spectrometer (PTR-MS, Ionicon) at JPAC. The technique is extensively described in the literature[39]. Calibrations were performed by diffusion sources[40] for α-pinene and the other reactants used. The PTR-MS was switched every 25 min between the inlet and the outlet of JPAC. The sampling lines consisted of ~10-m-long PFA tubing of 4 mm i.d. and were heated to 60 °C. The sampling flow rate was 500 ml min^{-1}.

The chemical composition of the particles in JPAC was determined on-line using an aerosol mass spectrometer (HR-ToF-AMS, Aerodyne Research). The HR-ToF-AMS was connected to the reaction chamber via stainless steel tubing (~3 m with 10 mm i.d. followed by ~1.5 m with 4 mm i.d., the 10 mm line was pumped with 2 l min^{-1}). The HR-ToF-AMS working principles and modes of operation are explained in detail elsewhere[41,42]. Particles with vacuum aerodynamic diameters between 60 and 600 nm were focused by an aerodynamic lens, and vaporized at about 600 K with subsequent electron impact ionization (70 eV). The resulting fragment cations were recorded using a time of flight (ToF) mass spectrometer.

As the efficiency at which the AMS vaporizes pure ammonium sulphate particles can differ from the efficiency of vaporizing such particles coated with organics, we used the SMPS data in conjunction with the AMS data to acquire time traces for SOA and ammonium sulphate. The AMS organic and ammonium sulphate signals were used to calculate a particle density, with which we converted the total particle volume measured by the SMPS to total particle mass. Finally, the SOA to ammonium sulphate ratio from the AMS was used to split the total particulate mass into SOA mass and ammonium sulphate mass. The O/C and H/C elemental ratios were calculated using improved calibration values by M.C. *et al.* (manuscript in preparation).

We measured number size distributions of particles in the 1–3 nm range using a particle size magnifier (PSM[43]) in JPAC. The PSM uses highly supersaturated diethylene glycol vapour (DEG) to grow particles/clusters/molecules through condensation. The particles grow to roughly 100 nm before the condensing vapours are depleted, and thereafter the particles are counted by a condensation particle counter (CPC). In this work, a TSI 3785 CPC was used. Nano-condensation nuclei (nano-CN[24]) is used as a collective term for small particles, clusters and molecules that can activate and grow through condensation.

The ability to act as nano-CN is strongly governed by size, with activation becoming easier as particles become larger[43,44]. By scanning the DEG supersaturation in the PSM, the size cut-off can be varied, and by the change in concentration as a function of supersaturation, a size distribution can be achieved. However, the activation is also a function of composition, and although the PSM can be calibrated for certain compounds to achieve a supersaturation–size relationship, the calibration compounds are typically inorganic, and organic compounds may have very different activation behaviour[44]. The particles studied in this work are organic, and therefore no exact size information can be given. The supersaturation was tuned such that it was very close to the limit where DEG nucleates homogeneously, and we estimate that the lowest detectable size is slightly below 1.5 nm in mobility diameter, which corresponds to 400–1,000 Da depending on the density[45]. The size corresponding to the lowest supersaturation scanned is estimated to be 3 nm.

In Fig. 2d, particles larger than 3 nm are presented. This size is based on the above argument, and whether the actual size cut was 2.5 or 4 nm will not change the conclusions drawn from the data. In Extended Data Fig. 4a–e, the smallest size bin calculated from the PSM data are used, and it is reported as particles smaller than 1.5 nm.

ELVOC detection and quantification using the CI-APi-TOF. Ehn *et al.*[30] reported the detection of highly oxidized multifunctional (HOM) compounds, detected from both pinene oxidation experiments and ambient air, many of which had identical elemental formulas to the ELVOCs detected in this work. The HOM

observations were based on measurements of naturally charged ions with an APi-TOF, that is, no active ionization mechanism was employed. In this work we have chosen to use 'ELVOC' instead of 'HOM', as the volatility is the more important aspect of the molecules in question. The nitrate ion CI-APi-TOF spectra are very similar to the natural ion spectra because HNO_3 is often the most abundant strongly acidic gas phase species. This means that whenever ions are formed in the atmosphere due to energetic particles from cosmic rays or radioactive decay of, for example, radon, the negative ions will quickly (in <1 s typically) collide with HNO_3 to form NO_3^-. This results in all further ionization steps being similar to that occurring in the nitrate ion CI-APi-TOF. The main difference is that the reaction times in the atmosphere are much longer, and highly variable, making quantification of neutral ELVOCs impossible. Zhao *et al.*[46] have also recently used nitrate chemical ionisation to study VOC oxidation, and found large similarities between these natural ion measurements and their chemical ionization generated spectra, though they were unable to determine the elemental composition of the ions.

ELVOCs have thus been detected with several instruments, using active nitrate ionization or direct sampling of ambient ions without any sample treatment, as well as under both laboratory and field conditions. These findings have all yielded concentration estimates of the same order, and the dynamics of these molecules found in this work clearly require extremely low-volatility compounds, whereby we conclude that the ELVOCs cannot purely be the result of instrumental artefacts.

The sensitivity of the CI-APi-TOF to a compound X in the JPAC chamber is defined by the calibration factor C_X, as

$$[X] = C_X \times \frac{\sum_{i=0}^{2}\left[(HNO_3)_i(NO_3^-)(X) + (HNO_3)_i(X-H)^-\right]}{\sum_{i=0}^{2}(HNO_3)_i(NO_3^-)} \equiv C_X \times A$$

where [X] is the concentration of the neutral compound to be measured, and the numerator on the right hand side is the sum over all detected ion clusters containing the compound X, either as the neutral molecule or the deprotonated ion $(X–H)^-$. The denominator is the sum over all measured reagent ions. The ratio A is found from the measured spectra. [X] refers to the concentration in the chamber, which is the value we are interested in. However, diffusion losses in the inlet tubing will influence the actual concentration entering the charging region. We define the transmission of the sampling tubing as f_{inlet}, for example, if 60% of X is lost before reaching the charger, $f_{inlet} = 0.4$. In general, $[X]_{charger} = f_{inlet} \times [X]_{chamber}$.

The chemical ionization inlet was constructed for measurements of H_2SO_4, and the calibration coefficient can be determined by introducing a known amount of H_2SO_4 to the sample[47]. The structures of the newly detected ELVOCs are not yet determined, and therefore a direct calibration using an ELVOC standard is not possible. We employed several methods, both empirical and theoretical, to estimate the sensitivity of the CI-APi-TOF to ELVOCs (C_{ELVOC}).

It has been found[48] that the charging efficiency of H_2SO_4 is equal to the collision frequency of the nitrate (cluster) ions with H_2SO_4. The nitrate dimer ($HNO_3 \cdot NO_3^-$) is an extremely stable cluster, and therefore the chemical ionization source is very selective towards which molecules will be charged[33]. Strong acids can become charged through proton transfer, while some form clusters without charge transfer, where the clusters need to be even more strongly bound than the pure nitric acid–nitrate cluster ions. As we detect large ELVOC $\cdot NO_3^-$ signals, this suggests that the ELVOC $\cdot NO_3^-$ clusters are very stable. We assume that ELVOCs charge at their collision frequency with nitrate ions and that once such a cluster forms, it will not break apart during the short residence time in the charger. If they do not charge at the collision limit, or if they are only weakly bound, our detection efficiency (ion count rate per ELVOC number density) would be lower than we assume. Thus, this assumption provides a lower limit to the reported concentration of ELVOCs.

The theoretical maximum sensitivity is limited by the amount of ion collisions in the charger during the 200 ms residence time (RT). The reaction where $(HNO_3)_x(NO_3^-)$, $x = 0–2$, reacts with H_2SO_4 to produce $(HNO_3)_x(HSO_4^-)$ has been found to proceed at the collision limit, with experimentally determined rate coefficients[48] of $k_{ion} = (1.7–2.3) \times 10^{-9}\ cm^3\ s^{-1}$. Using this range of collision frequencies, the resulting collision limited calibration factor for H_2SO_4, C_{H2SO4}, including inlet losses, can be calculated:

$$[H_2SO_4]_{chamber} = C_{H2SO4} \times A\ , \quad A = k_{ion}[H_2SO_4]_{charger} \times RT$$

$$\Rightarrow C_{H2SO4} = \frac{[H_2SO_4]_{chamber}}{A} = \frac{[H_2SO_4]_{chamber}}{k_{ion}[H_2SO_4]_{charger} \times RT}$$

$$= \frac{[H_2SO_4]_{chamber}}{k_{ion} f_{inlet}[H_2SO_4]_{chamber} \times RT} = \frac{1}{f_{inlet} k_{ion} \times RT}$$

$$= \frac{1}{f_{inlet} \times (1.7-2.3) \times 10^{-9} cm^3 s^{-1} \times 0.2 s} = \frac{(2.2–2.9) \times 10^9 cm^{-3}}{f_{inlet}}$$

Using a CI-APi-TOF identical to the one in this study, and a sampling inlet for which we estimate $f_{inlet} \approx 0.7$, Jokinen *et al.*[11] reported $C_{H2SO4} = 1.3 \times 10^{10}\ cm^{-3} / 0.7 = 1.89 \times 10^{10}\ cm^{-3}$. Other losses of H_2SO_4 that were not accounted for may explain the slight deviation from collision limited charging.

To obtain C_{ELVOC} from the collision limited C_{H2SO4} calculated above, we need to estimate k_{ion} also for ELVOCs. Based on the chemical understanding of their formation mechanisms provided in this work, we assumed some possible structures and calculated the corresponding dipole moments and polarizabilities. Using the formulation of Su and Bowers[49], the collision frequencies of $(HNO_3)_x(NO_3^-)$, $x = 0–1$, with ELVOCs were calculated and compared to those of nitrate clusters with H_2SO_4. We found $k_{ion} = (1.5–2.8) \times 10^{-9}\ cm^3\ s^{-1}$ for ELVOCs, and $k_{ion} = (1.5–2.5) \times 10^{-9}\ cm^3\ s^{-1}$ for H_2SO_4 (in good agreement with the experimental values), and conclude that the collision frequencies can be assumed equal. We thus conclude that the maximum sensitivity, corresponding to the minimum ELVOC concentrations, can theoretically be constrained to $C_{ELVOC} = C_{H2SO4} = (2.2–2.9) \times 10^9 / f_{inlet}$. The inlet line used in this work was about 80 cm (10 mm o.d. stainless steel tubing) which yields a diffusion limited loss in the inlet tubing of ~40% ($f_{inlet} \approx 0.6$). We can thereby provide a lower theoretical bound of $C_{ELVOC} = (0.4–0.5) \times 10^{10}\ cm^{-3}$, while the corresponding upper bound is roughly $9.5 \times 10^{10}\ cm^{-3}$ (as larger values would result in limonene ELVOC yields >100%, see Extended Data Fig. 5).

For comparison, we also calibrated to a large perfluorinated carboxylic acid, which was detected at times in the CI-APi-TOF spectra, presumably related to the addition of new Teflon tubing to the chamber. We used a gravimetrically calibrated permeation source of perfluoroheptanoic acid (PFHA) and found $C_{PFHA} = (1.6 \pm 0.4) \times 10^{10}\ cm^{-3}$. Given the large gas-phase acidity of such compounds, we expect that it forms a stable cluster with the nitrate ion near the theoretical collision limit. The largest contribution to the uncertainty in C_{PFHA} is due to measurements of the minuscule weight loss of the source over time.

The calibration factor $C_{PFHA} = (1.6 \pm 0.4) \times 10^{10}\ cm^{-3}$ agrees well with C_{H2SO4} reported[11] for a similar CI-APi-TOF, and therefore we also used $C_{ELVOC} = 1.6 \times 10^{10}\ cm^{-3}$ for converting ion counts to ELVOC concentrations.

We estimate a total uncertainty in C_{ELVOC} based on individual uncertainties in the measurements and above calculations (see Extended Data Fig. 6a). The total uncertainty was calculated using the propagation of uncertainties:

$$\delta = \sqrt{\delta_{CF}^2 + \delta_{TE}^2 + \delta_{WL}^2 + \delta_{RT}^2}$$

$$= \sqrt{(0.18)^2 + (0.33)^2 + (0.25)^2 + (0.25)^2} = 0.52$$

We therefore estimate a ±50% uncertainty in reported concentrations, but note again that if anything, our assumptions lead towards a lower limit estimate of ELVOC concentrations.

Steady state chamber measurements and yield calculations in JPAC. The average residence time in JPAC with respect to flush-out was 45 min. All results presented in this study are from steady-state measurements, which means that the inflow of all gases, oxidants, VOCs and so on were kept constant, as were all photolysing lights (if in use). These conditions were maintained until all relevant compounds (such as VOCs, ELVOCs, particles) were constant in the chamber (and thereby also the outflow). Under steady state conditions, the rate of change of a compound X is zero, and we can write

$$\frac{d[X]}{dt} = \sum_i Q_i - \sum_j L_j = 0$$

where Q_i and L_j are the sources and sinks for X, respectively.

For ELVOC formation during α-pinene ozonolysis, we find that the source can be written $k_1 \gamma [\alpha\text{–pinene}][O_3]$, where k_1 is the (known) reaction rate coefficient for α-pinene with ozone, and γ the fraction of that reaction producing ELVOCs, which we define as the molar yield. The loss of ELVOCs was determined from the reciprocal of the lifetime, which was found to be ~90 s based on following their decay after turning off the ELVOC sources (see below). Flush-out from the chamber corresponds to a lifetime of 45 min, and the condensation sink (that is, loss rate to particles) was generally even slower during the ozonolysis experiments without seed, and therefore we presume that the 90 s lifetime correspond to loss at the chamber walls. We thus write

$$\frac{d[ELVOC]}{dt} = k_1 \gamma [\alpha\text{–pinene}][O_3] - k_{loss}[ELVOC] = 0$$

$$\Rightarrow \gamma = \frac{k_{loss}[ELVOC]}{k_1[\alpha\text{–pinene}][O_3]}, \quad k_1 = 8.66 \times 10^{-17} cm^3 s^{-1}, \quad k_{loss} = \frac{1}{90 s} = 0.011 s^{-1}$$

where the final denominator is the α-pinene ozonolysis rate (x axis in Fig. 2a), and [ELVOC] is the steady-state concentration of ELVOCs, plotted on the y axis in

Fig. 2a. Thus, to calculate the ELVOC molar yield, one only needs to account for k_{loss}, which for all practical purposes can be assumed constant. In Fig. 2a, all points fall between the lines depicting molar yields of 6 and 8%.

To calculate the corresponding ELVOC mass yield, we need the signal-weighted average molar mass of the ELVOCs, $\langle M_{ELVOC}\rangle$, which is found to be ~325 Da. It follows that

$$\gamma_{mass} = \frac{m_{ELVOC}}{m_{\alpha-pinene-reacted}} = \frac{n_{ELVOC} \times \langle M_{ELVOC}\rangle}{n_{\alpha-pinene-reacted} \times M_{\alpha-pinene}}$$
$$= \gamma \frac{\langle M_{ELVOC}\rangle}{M_{\alpha-pinene}} = \gamma \frac{325\,Da}{136\,Da} = 2.4\gamma$$

which shows that the mass yield is roughly 2.4 times larger than the molar yield, due to the incorporation of the oxygen molecules in the ELVOCs. However, this relation of 2.4 only holds for the α-pinene ozonolysis ELVOC spectrum under the conditions in JPAC, as the average molar mass will vary according to the spectral features. JPAC has an average residence time of 45 min, which makes the study of processes occurring on shorter timescales challenging. However, using the near-instantaneous response of OH concentrations to turning ultraviolet lights on and off can be used for specific tests. Certain ELVOCs are produced mainly from ozonolysis, and others mainly from OH oxidation, with the most abundant compound detected during ozonolysis being $C_{10}H_{14}O_7$ and during (low-NOx) OH oxidation $C_{10}H_{16}O_7$. To probe the loss rate of ELVOCs, we let the chamber conditions reach steady-state during OH oxidation with ultraviolet lights on, and then monitored the decay of the OH-produced ELVOCs after turning off the ultraviolet lights. After about 5 min, the ultraviolet lights were turned back on, and the chamber again reached steady-state in less than an hour, and the experiment could be repeated. A cycle of three such decay experiments are plotted for selected OH-produced ELVOCs in Extended Data Fig. 6b. In Extended Data Fig. 6c all three decay periods are plotted on a logarithmic scale relative to the instant when the ultraviolet light was switched off. The dashed and dotted lines correspond to lifetimes (τ) of 90 and 75 s, respectively. The upper bound of 90 s was used in this work to provide a conservative estimate of ELVOC yields. During these experiments, the calculated loss rate to particles (that is, the condensation sink) corresponded to clearly longer lifetimes ($\tau > 300$ s).

The decay in Extended Data Fig. 6c clearly follows an exponential trend, as expected, which can be followed over a period of $>2\tau$. The acquired lifetimes of 75–90 s are in line with what would be expected in an actively mixed chamber of ~1.5 m^3.

The condensation sink (that is, loss of ELVOCs to particle surface area), was calculated using a standard approximation to the Fuchs-Sutugin formulation of gas-diffusion limited collision and accommodation at the particle surface. We calculated a gas-phase diffusivity of ELVOCs (of the order of 0.05 $cm^2\,s^{-1}$) from the measured molecular mass and found that to describe the decay of ELVOC signal with increasing particle surface area, we require a mass accommodation coefficient of unity.

At low particle loadings, the dominant sink for ELVOCs in JPAC was diffusional loss to chamber surfaces. This loss rate of 1/(90 s) = 0.011 s^{-1} (see above) roughly equals the condensation sink from 200 nm particles at a concentration of 4,000 cm^{-3}. This, in turn, corresponds to a rather large mass loading of seed particles, about 25 $\mu g\,m^{-3}$, being required to equal the wall loss rate. The need to account for vapour–wall interactions has been acknowledged in recent studies, both from the point of view of SVOC partitioning[50,51], as well as for irreversibly condensing vapours[52] such as ELVOCs.

During experiments where seed aerosol was added, the condensation sink (CS) was increased to be competitive with the wall loss. In Fig. 2c, we plot the predicted ELVOC concentration and the SOA from ELVOC condensation (SOA_{ELVOC}) as functions of total particle surface area. The condensation sink for ELVOCs to particles is added to the loss terms for ELVOCs and by definition becomes a source term for SOA_{ELVOC}:

$$\frac{d[ELVOC]}{dt} = k_1\gamma[\alpha-pinene][O_3] - (k_{loss} + CS)[ELVOC]$$
$$\equiv Q_{ELVOC} - (k_{loss} + CS)[ELVOC] = 0$$
$$\frac{d\,SOA_{ELVOC}}{dt} = CS[ELVOC] - k_{fo}SOA_{ELVOC} = 0$$

where k_{fo} is the flush-out rate, equal to the reciprocal of the chamber residence time of ~45 min, which we determined to be the dominant loss for particles larger than 10 nm. We note that at very low particle surface, we can write $Q_{ELVOC} = k_{loss}[ELVOC]_{CS=0}$, and as both equations above contain the ELVOC condensation rate, CS[ELVOC], we can predict [ELVOC] by

$$[ELVOC] = \frac{Q_{ELVOC}}{(k_{loss} + CS)} = \frac{k_{loss}[ELVOC]_{CS=0}}{(k_{loss} + CS)} = \frac{[ELVOC]_{CS=0}}{\left(1 + CS/k_{loss}\right)}$$

and SOA_{ELVOC} from

$$Q_{ELVOC} - k_{loss}[ELVOC] = k_{fo}SOA_{ELVOC}$$
$$SOA_{ELVOC} = \frac{Q_{ELVOC} - k_{loss}[ELVOC]}{k_{fo}} = \frac{k_{loss}}{k_{fo}}\left([ELVOC]_{CS=0} - [ELVOC]\right)$$

In other words, SOA_{ELVOC} increases as [ELVOC] decreases, as expected, and the observed 'concentration enhancement' follows the ratio of the loss rates of ELVOCs (k_{loss}) and SOA (k_{fo}).

The predicted ELVOC concentrations tracked the observations very well (Fig. 2c). The prediction of SOA mass also tracked the measurements, with deviations increasing at higher loadings, indicating that SOA_{ELVOC} constituted a major fraction of the total SOA under all conditions probed. At higher loadings, other sources of SOA apparently became more pronounced. As noted in the main text, and shown in Extended Data Fig. 3, the O/C and H/C ratios measured in the SOA by an AMS were in good agreement with those calculated from the measured ELVOCs that had been lost upon seed addition. We also note that the ELVOCs detected by the nitrate CI-APi-TOF were essentially the only gas-phase compounds observed to decrease upon seed addition. None of the more abundant compounds detected by the UW HR-ToF-CIMS that have compositions consistent with more common SVOC products, such as pinonic and pinic acids, showed any noticeable perturbation by the presence of seed (Extended Data Fig. 2b).

The SOA mass yields presented in the paper were calculated as the ratio of SOA formed to VOC reacted. It is important to note that the SOA mass yield is calculated from the total reacted α-pinene, whereas the ELVOC yield is a branching ratio of the specific α-pinene+ozone reaction. In the experiments presented in Fig. 2b, the input flow to the chamber contained 34 p.p.b. α-pinene, whereas the outflow, and thus the steady-state concentration in the chamber, was 19 p.p.b. (see Extended Data Fig. 6d). During the 45 min average residence time, 15 p.p.b. α-pinene reacted, which corresponds to 85 $\mu g\,m^{-3}$. Before seed addition the AMS-measured SOA mass was ~1.1 $\mu g\,m^{-3}$, and afterwards it had increased to ~8.8 $\mu g\,m^{-3}$. These values thus correspond to SOA mass yields of 1.3% and 10.3%, respectively. The yield of 10% is similar to, or still slightly lower than, those reported for low loadings by Shilling *et al.*[16], who also used steady-state chamber conditions and added seed aerosol. However, direct comparisons to other chamber studies are difficult, due to differences in chamber size and operation (steady state versus batch reactor, seed versus no seed, use of an OH scavenger, active mixing, and so on). At low loadings, in particular, the role of wall losses for both ELVOCs and particles becomes more important to diagnose and quantify relative to the condensation sink provided by seed particles.

Ambient growth rate calculations. Growth rates were calculated from particle formation events observed in Hyytiälä during spring 2011. Log-normal distributions were fitted to measured particle number size distributions and the growth of the newly formed particles was followed using the geometric mean diameters of the fitted modes (d_p). The diameter growth rate GR = dd_p/dt is calculated by numerically differentiating the d_p time series. An example of a particle formation and growth event together with the mean diameters of the fitted modes (black dots) is shown in Extended Data Fig. 8.

The particle diameter growth rate (GR) can also be calculated as a function of vapour concentration (C_v) using the expression below[53]:

$$GR = \gamma \frac{m_v}{2\rho_v}\left(\frac{8kT}{\pi m_v}\right)^{1/2}\left(1 + \frac{d_v}{d_p}\right)^2 C_v\,, \qquad \gamma = \frac{4}{3}Kn\,\beta_m$$

where m_v, d_v and ρ_v are the molecular mass, diameter and condensed-phase density of the vapour, respectively. Kn is the Knudsen number and β_m the Fuchs-Sutugin transition regime correction factor for mass flux. Using the above equation we can calculate the growth rates corresponding to the measured vapour concentrations C_v. For the ELVOCs we assumed molecular mass m_v = 300 Da, ρ_v = 1.5 g cm^{-3} and d_v = 0.9 nm. With these assumptions, an ELVOC concentration of 1 p.p.t. corresponds to a GR of roughly 2 nm h^{-1} for a 25-nm particle.

The average measured growth rate from 5 to 50 nm (or as high as the mode of new particles could be followed, if <50 nm) for the five particle formation events detected during the 2011 deployment[11] of the CI-APi-TOF in Hyytiälä were compared to the growth rate expected from the average ELVOC concentration measured during the events (Fig. 3). The agreement is extremely good, considering the uncertainties involved, as well as the fact that the particles have grown in the air parcel over a period of 12–24 h, and we are comparing to stationary ELVOC measurements at Hyytiälä. However, the critical finding is that the ELVOC concentrations in this region are indeed of the correct order to explain the major part of the observed growth of new particles.

ELVOC formation mechanism hypothesis. Without structural information on the ELVOCs, unambiguously determining their formation mechanism is not possible. However, we performed a range of experiments as well as model calculations to understand the chemical properties of ELVOC and the sensitivity of their formation to various atmospheric conditions. This information allowed us to formulate a hypothesis, which provides a formation pathway from VOCs to ELVOCs, that is consistent with all our experimental findings, and is supported by model calculations. This pathway relies on known chemistry, albeit with certain pathways increasing in importance compared to current mechanisms.

Peroxy radicals (RO_2) are typical intermediates in most VOC oxidation reactions, also in the case of α-pinene ozonolysis. We can explain ELVOC formation in this system by a fraction of the initial RO_2, formed upon ozonolysis, undergoing fairly rapid ($\sim 1\ s^{-1}$) sequential intramolecular H-atom abstractions (H-shifts[19,20,54–57]), each followed by O_2 addition at the formed alkyl radical site (Extended Data Fig. 9a). With each net abstraction-addition step, a hydroperoxide moiety is formed, and a new peroxy radical group arises on the C-atom where the hydrogen abstraction took place. Hydrogen shift reactions are well known in the atmospheric chemical literature[19,54–57] but these reactions have generally been thought to terminate through unimolecular decomposition by loss of CO or OH[58,59] before reaching oxygen contents as high as those in the molecules we have detected.

ELVOC monomers, such as those presented in Fig. 1, can form through reactions of highly oxygenated peroxy radicals ($R_{ELVOC}O_2$) with RO_2, HO_2 or NO, either directly or via further alkoxy radical pathways, as summarized in Extended Data Fig. 9b, c. The ELVOC dimers (Fig. 1) appear to form only through reactions of $R_{ELVOC}O_2$ with other $R'O_2$ (not necessarily another $R_{ELVOC}O_2$) to form an organic peroxide ROOR′. The proposed formation of organic peroxides from RO_2 cross reactions is not new[60], yet it is often ignored as a minor channel[54,55]. This may be based on experiments using small RO_2, whereas recently C_5 peroxy radicals were found to have ROOR yields of several percent, and the yield is expected to increase for larger RO_2 due to more vibrational modes available to distribute collisional energy and thereby prevent the molecules from breaking apart[61].

The presence of oxygenated functional groups is known to increase both the equilibrium constants and the rates of H-shifts significantly, as shown by both *ab initio* calculations[19,20,62,63] and recent experiments[20]. This helps explain why alkenes with endocyclic double bonds, such as α-pinene, have high ELVOC yields from ozonolysis. In such molecules, the breaking of the double bond does not generally cause fragmentation, and therefore the formed RO_2 will be more functionalized than a corresponding RO_2 from a non-cyclic alkene. A more detailed description, as well as experiments using cyclic and non-cyclic alkenes, are discussed below in the section 'Supporting experiments for the sequential H-shift mechanism'.

The sequential H-shift mechanism competes with decomposition channels, which may terminate the radical propagation chain, thus preventing further O_2-additions and subsequent H-shifts to form $R_{ELVOC}O_2$. The relative rates of H-shifts and decomposition reactions depend on the specific structure of the initial peroxy radical, and thus the parent VOC. For example, if an H-shift occurs from an aldehyde, O_2 addition (and subsequent H-shifts) will then compete with CO elimination from the resulting $RC^{\bullet}=O$ radical[64]. If the radical centre is significantly stabilized by neighbouring functional groups, CO loss is likely to be fast[58,59,64]. In the absence of such stabilization, for example, if the $RC^{\bullet}=O$ radical is adjacent to a CH_2 group, CO loss will probably not be competitive with O_2 addition, which occurs at an effective rate of $5\times10^{7}\ s^{-1}$ at an O_2 concentration of 0.2 atm (ref. 65). The latter situation applies for example, certain α-pinene-derived peroxy radicals. If the carbonyl adjacent to the original peroxy group (now a COOH group) is also an aldehyde, a second hydrogen abstraction from this aldehydic carbon will be rapid, and very probably competitive with other favourable abstraction sites, such as the COOH carbon and possible tertiary alkyl carbons[59,63]. The $R_1R_2C(OOH)C^{\bullet}=O$ radical thus formed will probably either decompose with a loss of CO (and subsequent loss of OH from the $R_1R_2C^{\bullet}OOH$ radical), or add O_2, forming a peroxy radical with four oxygen atoms more than the original RO_2. In the absence of bimolecular loss reactions, this basic mechanism of O_2 addition and subsequent H-shifts can then continue until a hydrogen is abstracted at a COOH carbon, leading to immediate OH loss[58].

Direct $R_{ELVOC}O_2$ detection and dependence on NO and total RO_2. When charged by the nitrate ion (NO_3^-), the majority of ELVOCs are detected at even integer masses, as expected for closed shell organic molecules containing only C, H and O. There are, however, ions that emerge at odd integer masses, and behave differently than the rest of the ELVOCs. The elemental composition of these ions can be unambiguously determined owing to the high resolution of the CI-APi-TOF, and they are found to contain an odd number of H-atoms, indicating radical species. The behaviour of these odd mass ions during our experiments was always consistent with that expected from highly oxidized peroxy radicals, as shown below.

With varying monoterpene (MT) oxidation rates, $[MT]\cdot[O_3]$, the ELVOCs (both monomers and dimers) exhibit a near linear dependence (as shown in Fig. 2). In contrast, $R_{ELVOC}O_2$ radicals, such as $C_{10}H_{15}O_{10}^{\bullet}$, are observed to follow a square-root behaviour (Extended Data Fig. 10a). Such a dependence is also expected, if the dominant loss of $R_{ELVOC}O_2$ and other RO_2 is reaction with other peroxy radicals. In many systems, dimer concentrations behave as the square of the monomer concentration, but in this case, the similar behaviours of the monomer and dimer are consistent with both forming in part from $RO_2 + R_{ELVOC}O_2$ reactions. Reactions such as those between a Criegee intermediate (CrI) and closed shell products[66] are expected to lead to higher order dependencies than observed in Extended Data Fig. 10a. This specific mechanism[66] would also not produce the high oxygen content we observe in the detected ELVOCs. However, while we are not sensitive to less oxidized products, such CrI reactions may still be taking place.

Extended Data Fig. 10b shows the behaviour of three ELVOCs, a monomer, dimer and an organic nitrate ($RONO_2$), as a function of the corresponding $R_{ELVOC}O_2$ radical $C_{10}H_{15}O_{10}^{\bullet}$ during an experiment where α-pinene and ozone concentrations were kept constant, while varying the amount of NO in the chamber. We added NO_x to the chamber and used the 365 nm UV-A lamps to photolyse NO_2 to NO ($J_{NO2}\approx 4.3\times10^{-3}\ s^{-1}$) to compensate for the reaction $NO + O_3 \rightarrow NO_2 + O_2$. The NO concentrations were calculated using the amount of NO_x added to the chamber from a calibrated cylinder and a photostationary state assumption, which carries more uncertainty compared to a direct measurement of NO which was not available. As an example, at 100 p.p.b. O_3, steady-state $NO/NO_2 \approx 10\%$ in the chamber.

The calculated NO (red markers and red line fit) is shown in Extended Data Fig. 10b with the same species shown in **a** as well as an $RONO_2$ detected by the CI-APi-TOF. The same data are shown in Extended Data Fig. 10c against a smoothed interpolation of the calculated NO concentration. Increasing NO causes a clear drop in $C_{10}H_{15}O_{10}^{\bullet}$ and other $R_{ELVOC}O_2$ and an increase in the corresponding $RONO_2$ ($C_{10}H_{15}NO_{11}$, blue dots), as expected due to increased $R_{ELVOC}O_2 + NO$ reactions. As the NO reached about 1 p.p.b., the ELVOC dimers (light green dots) reached zero, consistent with $R_{ELVOC}O_2 + RO_2$ reactions becoming negligible due to titration of RO_2 by NO. However, $C_{10}H_{14}O_9$ decreases nearly linearly with decreasing $C_{10}H_{15}O_{10}^{\bullet}$, indicating that it forms from reactions with both RO_2 and NO. Both these reactions can produce alkoxy radicals (RO), and therefore we expect $C_{10}H_{14}O_9$ to be a product of this pathway.

The $RONO_2$, $C_{10}H_{15}NO_{11}$, increases with NO at low NO concentrations, but eventually reaches a maximum and consequently decreases with further increase of NO. If the source of $R_{ELVOC}O_2$ were independent of NO, then at high NO, practically all $R_{ELVOC}O_2$ should react with NO and the $RONO_2$ concentrations should stay constant since its formation rate is the product $[R_{ELVOC}O_2]\times[NO]$. However, the decrease of $C_{10}H_{15}NO_{11}$ at high NO is consistent with the less oxygenated RO_2 reacting with NO before having time to perform intramolecular H-shifts and thereby form highly oxygenated $R_{ELVOC}O_2$.

We constructed a simplified kinetic box model with the aim of reproducing these observations (that is, Extended Data Fig. 10a–c) using a minimal amount of reactions similar to those summarized in Extended Data Fig. 9b, c . The only non-standard components of the mechanism are that (1) a fraction of RO_2 produced upon monoterpene ozonolysis can undergo several intramolecular H-shift reactions followed by either O_2 addition or decomposition, and (2) $R_{ELVOC}O_2$ reactions with other RO_2 form ROOR dimer products at significant yields. For comparison, we also incorporated a similar mechanism into the detailed Master Chemical Mechanism (MCM) version 3.2 and found the same results. The key reactions used to model the ELVOC system are listed in Extended Data Fig. 7a. In the model, three H-shift reactions are required to form $R_{ELVOC}O_2$ (which in this case contains 10 O-atoms) in order to compare to Extended Data Fig. 10. However, the RO_2 formed after two H-shifts ($R'''O_2$) is also likely to produce some of the ELVOCs we observe. Parameters used for the model runs are shown in Extended Data Fig. 7b. The goal here is not to arrive at accurate rate coefficients or other mechanistic parameters, but rather to illustrate that the proposed mechanism is a reasonable hypothesis to describe ELVOC formation and behaviours. Extended Data Fig. 10d–f summarizes the box model predictions.

The model successfully reproduces the experiments without added NO_x (Extended Data Fig. 10d), showing both a qualitative and quantitative agreement with observations in Extended Data Fig. 10a. The increase of predicted $R_{ELVOC}O_2$ follows a square-root dependence while the closed shell ELVOC monomers and dimers increase nearly linearly. The model can also qualitatively reproduce the observations from experiments with NO_x addition (Extended Data Fig. 10e), such as those plotted in Extended Data Fig. 10b. As NO is increased, the predicted concentration of the $R_{ELVOC}O_2$ radical $C_{10}H_{15}O_{10}^{\bullet}$ also decrease, as expected (Extended Data Fig. 10f). The dimer decreases rapidly with increasing NO, while the monomer decreases much more slowly, and does not reach zero due to a source from $R_{ELVOC}O_2 + NO$. The organic nitrate first increases with increasing NO, but

eventually turns over and starts decreasing, consistent with the observations. To reproduce the turnover at the same point as in the observations, the H-shift reactions needed to occur at rates on the order of 1 s^{-1}, to allow NO reactions to compete.

The model predicts that at low NO (<1 p.p.b.), most of the first generation $R'O_2$ radicals capable of forming $R_{ELVOC}O_2$ still do so, and the majority of $R_{ELVOC}O_2$ react with NO, and therefore the organic nitrate concentration reaches a maximum. When increased above 1 p.p.b., NO scavenges some $R'O_2/R''O_2/R'''O_2$ radicals and thereby decrease the amount of ELVOC organic nitrates. Non-ELVOC nitrates may form instead, but those will be less oxidized and are not detected by the CI-APi-TOF, though some are detected by the UW HR-ToF-CIMS. A similar type of scavenging can also occur at very high RO_2 concentrations, with implications for chamber experiments.

In fact, this mechanism suggests that very high loadings of VOCs and/or NO_x can suppress $RO_2 \rightarrow R_{ELVOC}O_2$ conversion due to competing RO_2+RO_2 and RO_2+NO reactions, respectively, thereby changing the nature and possibly the inferred yield of SOA. Under such conditions, heterogeneous and condensed phase reactions[2,21,67–69] may become the dominant SOA sources even at lower SOA loadings. However, in the atmosphere, VOCs or NO will only rarely be present at high enough concentrations to compete with H-shift reactions of RO_2, and thus most oxidation processes able to form ELVOCs will do so in any rural or remote region. In general, the relative amounts of RO_2, HO_2 and NO will only influence the type of ELVOCs (monomers, dimers, nitrates) formed. As a direct example, the ratio of ELVOC dimers to monomers is higher during our α-pinene ozonolysis chamber experiments than in Hyytiälä at night, as expected due to RO_2/HO_2 ratios being higher in our chamber than in ambient air.

We note that the number concentration of particles <1.5 nm in size provides an independent measure of large molecular mass compounds (for example, ELVOC dimers). ELVOC monomers and dimers are formed through the same processes under low-NO_x conditions, making their decoupling challenging. However, by adding NO_x to the chamber we were able to perturb the ELVOC monomer to dimer ratio to separately elucidate their effect on the smallest particles detected by the PSM. Extended Data Fig. 4b–e illustrates that upon addition of NO_x (that is, NO), the concentration of particles smaller than 1.5 nm decreases. The decrease in $PSM_{<1.5nm}$ is nonlinearly related to ELVOC monomers and $R_{ELVOC}O_2$ (panels **a** and **c**), non-monotonically related to $R_{ELVOC}ONO_2$ (panel **b**), and linearly related to the concentration of ELVOC dimers. That is, the response of $PSM_{<1.5nm}$ is directly proportional to ELVOC dimers, which, in the presence of NO are nonlinearly related to $R_{ELVOC}O_2$ and ELVOC monomers. This is entirely consistent with the above mechanism whereby ELVOC monomers and dimers are produced from $R_{ELVOC}O_2$ chemistry.

Supporting experiments for the sequential H-shift mechanism. Ozono-alkene reactions are complex, and we will focus mainly on the steps relevant for ELVOC formation. For detailed discussions on the ozonolysis of unsaturated compounds, see for example, Johnson and Marston[70] or Vereecken and Francisco[71].

When ozone reacts with a double bond, it forms a primary ozonide (POZ) that quickly decomposes, resulting in a carbonyl and a Criegee intermediate. The chemistry of Criegee intermediates are discussed extensively elsewhere[70,71], and we will only focus on the major decomposition pathway, which forms an alkyl radical that reacts with O_2 to form a peroxy radical[70–73]. Of the three O-atoms in the reacted ozone, one has been lost as the hydroxyl radical (OH), one is left in a carbonyl in the co-product, and one is incorporated as a carbonyl in R in the peroxy radical RO_2. In the case of a cyclic alkene like α-pinene (Extended Data Fig. 5a), both carbonyls will be left in R. According to our hypothesis, the rest of the oxygen addition required to form ELVOCs occur via addition of O_2.

To validate both the initial ozone reaction, as well as the further O-atom additions purely by incorporation of O_2, we used isotopically labelled $^{18}O_3$ to initiate the ozonolysis reaction in the Tropos flow tube. As seen in the example spectra in Extended Data Fig. 1c, all ELVOC monomers, both the RO_2 radical at 357 Th ($C_{10}H_{15}O_{10}^{\bullet}$) as well as the other closed shell monomers at 340 ($C_{10}H_{14}O_9$) and 342 ($C_{10}H_{16}O_9$), shift by 4 Th, in accordance with only two O-atoms from ozone becoming incorporated into the ELVOCs. Furthermore, Extended Data Fig. 1d shows that the dimers shift by 8 Th, as expected from reactions between $R_{ELVOC}O_2$ and RO_2, where both radicals bring two labelled O-atoms to the molecule $R_{ELVOC}OOR$.

It should also be noted that in similar experiments where sulphur dioxide (SO_2) was added, the oxidation of SO_2 by OH and/or Criegee intermediates[74] produced HSO_4^- signals that were shifted by 2 Th. This further suggests that no additional reactions with oxidants are required in ELVOC formation, as this would cause larger shifts in the ELVOC spectra than now observed.

We used cyclohexene (Ch, Extended Data Fig. 5a), C_6H_{10}, as a surrogate for endocyclic alkenes in order to further test our hypothesis. Ch produced ELVOCs efficiently upon ozonolysis, with the dominant detected monomer being $C_6H_8O_9$. We conducted experiments using this surrogate and other related alkenes to test whether ELVOC formation was affected by excess internal energy associated with the CrI, the presence of oxygen-containing functional groups in the RO_2, and/or the presence of deuterium.

At the step where the POZ formed in Ch ozonolysis decomposes, we end up with a non-cyclic, six-carbon chain with the CrI on one end and a carbonyl on the other. For comparison, 6-nonenal (Extended Data Fig. 5a), a straight chain C_9 alkene with a carbonyl group on the first C-atom, produces two separate (C_3 and C_6) molecules upon ozonolysis. When the CrI is left on the C_6 product, we expect the identical CrI as formed from Ch, and we indeed observed an ELVOC spectrum similar to that of Ch, with the dominant peak found at $C_6H_8O_9$. This result is important, as it shows that the high internal energy remaining in the CrI from Ch is not a requirement for ELVOC formation, as some of that energy is lost in the 6-nonenal case as kinetic energy in the C_3 and C_6 fragments.

We also reacted 1-heptene (Extended Data Fig. 5a) with ozone, and in this case, the decomposition of the POZ will form a C_1 and a C_6 molecule. The main difference between the C_6 molecules with CrI functionalities formed from Ch or 6-nonenal, and that of 1-heptene, is that the former has the additional carbonyl in the other end of the molecule. Our results clearly show that ELVOCs form from Ch and 6-nonenal, while the ELVOC yield from 1-heptene is practically zero, suggesting that the 'extra' carbonyl functionality greatly enhances H-shift reactions in linear RO_2. This is in agreement with previous studies indicating that H-shifts from aldehydic carbons proceed rapidly[59,63].

Although the fastest H-abstraction in the Ch RO_2 is from the aldehydic C-atom, it should be noted that also abstraction from C atoms next to carbonyl groups may be fairly rapid[20]. This suggests that for example, ketones, with no available hydrogen atoms on the carbonyl C, may still enhance the abstraction from the adjacent C-atoms. Such ketones can form in, for example, α-pinene ozonolysis upon ring-opening. In addition to H-atoms adjacent to oxidized C-atoms, other competitive hydrogen abstraction points are also available in peroxy radicals formed from α-pinene, namely the tertiary H-atom[63,75] on the 4-membered ring that results after ozonolysis. We speculate that the difference in ELVOC yields between α-pinene and Ch can be attributed to the more complex structure of α-pinene, where for example, tertiary C-atoms may provide more favourable H-abstraction spots. These experimental insights into the process support the hypothesis that intramolecular H-abstraction by oxygen-containing or branched RO_2 is a feasible functionalization process.

To further test the hypothesis of intramolecular H-shifts followed by O_2 addition, we also conducted experiments using deuterated cyclohexene (dCh, C_6D_{10}). Ozonolysis is only marginally slowed down by isotope effects[70]. However, H-shifts (or any reactions involving primarily the movement of hydrogen atoms) will be significantly slowed down when hydrogen atoms are replaced by deuterium. There are two main reasons for the slower reactions of deuterium atoms. First, H-shift reactions are typically associated with tunnelling factors well above 1, as hydrogen atoms are very light and thus able to quantum mechanically tunnel through potential barriers. Heavier deuterium atoms have much lower tunnelling factors, and thus deuterated molecules will have lower reaction rates. Second, the zero-point vibrational energy associated with X–D bonds is lower than that associated with X–H bonds (for any atom X). Thus, the energy needed to break X–D bonds is somewhat larger than that needed to break X–H bonds. For example, Crounse *et al.*[56] found that deuteration decreased the formation rate of H-shift products relevant to isoprene oxidation by a factor of around 15 at 298 K.

In agreement with the hypothesis of ELVOC formation involving sequential H-shifts, our results show that the ELVOC formation from dCh compared to Ch is slower by at least an order of magnitude, possibly even several orders of magnitude, but more exact numbers become difficult to quote due to the very low ELVOC yields from dCh. The first H-shift occurs already when the CrI decomposes to form the initial RO_2, and the slower deuterium abstraction may lead to enhanced secondary ozonide or dioxirane formation at the expense of RO_2 formation. According to our hypothesis, ELVOC formation should be slowed even further for each oxidation step following H-shifts. Thus, at the very least, these results show that the formation of the initial RO_2 is important, and if this step alone cannot explain the large observed drop in ELVOC formation, the subsequent H-shift reactions likely will.

ELVOC formation by OH oxidation. We also observed prompt ELVOC formation during OH oxidation experiments of α-pinene at a yield of roughly 1% (Extended Data Fig. 2a). This yield is much lower than that found for ozonolysis, and suggests that the role of ozone in forming low-volatility vapours has been underestimated. On the other hand, in similar experiments using pinonic acid, a semi-volatile first generation oxidation product with no reactivity towards ozone, ELVOC formation was also observed upon oxidation by OH (Extended Data Fig. 2c). In this case, the initial RO_2 will be functionalized, possibly enhancing the ELVOC formation. This further suggests that SVOC formed from both ozonolysis and OH

oxidation can form ELVOCs in subsequent oxidation steps. The extent to which first and second generation products of OH oxidation of VOCs contribute to ELVOCs thus requires further investigation. The evolution of SOA over timescales of hours to days, as discussed by Jimenez *et al.* [1] is further confirmation that multi-step reactions, probably in both the gas and particulate phase, influence SOA characteristics.

ELVOC yields from ozonolysis of other monoterpenes and alkenes. To show that endocyclic alkenes are indeed especially efficient at producing ELVOC, we compared the ELVOC ozonolysis yields of several monoterpenes and other VOCs. Here we present results from cyclohexene, α-pinene and two other atmospherically relevant monoterpenes: limonene and β-pinene (Extended Data Fig. 5a). The findings are summarized in Extended Data Fig. 5b. Although the other VOCs were not characterized to the extent of α-pinene, a clear trend was visible. Cyclohexene, which only contains a six-membered ring showed an ELVOC yield of 4%, which was slightly lower than that found for α-pinene. The difference can be attributed to the more complex structure of α-pinene, where for example, tertiary C-atoms may be more favourable for H-shifts. The limonene ELVOC yield was roughly twice that of α-pinene, and this high yield was probably influenced by the fact that limonene contains two double bonds, and can thus react twice with ozone during the residence time in our chamber. In other words, a large fraction of the first generation oxidation products that did not form ELVOCs can react once more with ozone (or OH) to produce ELVOCs. This leads to the high apparent yield of 17%, which in fact is a combination of both first and second generation ozonolysis products, and can therefore not be directly compared to the yields from other VOCs with only one double bond. A similar effect is seen in Extended Data Fig. 2a, where multiple OH reactions appear to increase the ELVOC yield. The ELVOC yield of β-pinene on the other hand was about 2 orders of magnitude lower than that of α-pinene. This large difference is readily explained by our hypothesis, where efficient sequential H-shift reactions will only take place if the double bond reacting with ozone is endocyclic. Thus these findings, as well as all findings using other tested precursors, are in agreement with our proposed mechanism for ELVOC formation.

31. Berndt, T., Boge, O., Stratmann, F., Heintzenberg, J. & Kulmala, M. Rapid formation of sulfuric acid particles at near-atmospheric conditions. *Science* **307,** 698–700 (2005).
32. Hari, P. & Kulmala, M. Station for measuring ecosystem-atmosphere relations (SMEAR II). *Boreal Env. Res.* **10,** 315–322 (2005).
33. Eisele, F. L. & Tanner, D. J. Measurement of the gas-phase concentration of H_2SO_4 and methane sulfonic-acid and estimates of H_2SO_4 production and loss in the atmosphere. *J. Geophys. Res.* **98,** 9001–9010 (1993).
34. Junninen, H. *et al.* A high-resolution mass spectrometer to measure atmospheric ion composition. *Atmos. Meas. Techniques.* **3,** 1039–1053 (2010).
35. Kirkby, J. *et al.* Role of sulphuric acid, ammonia and galactic cosmic rays in atmospheric aerosol nucleation. *Nature* **476,** 429–433 (2011).
36. Yatavelli, R. L. N. *et al.* A chemical ionization high-resolution time-of-flight mass spectrometer coupled to a micro orifice volatilization impactor (MOVI-HRToF-CIMS) for analysis of gas and particle-phase organic species. *Aerosol Sci. Technol.* **46,** 1313–1327 (2012).
37. Yatavelli, R. L. N. & Thornton, J. A. Particulate organic matter detection using a micro-orifice volatilization impactor coupled to a chemical ionization mass spectrometer (MOVI-CIMS). *Aerosol Sci. Technol.* **44,** 61–74 (2010).
38. Bertram, T. H. *et al.* A field-deployable, chemical ionization time-of-flight mass spectrometer. *Atmos. Meas. Techniques* **4,** 1471–1479 (2011).
39. Lindinger, W., Hansel, A. & Jordan, A. On-line monitoring of volatile organic compounds at pptv levels by means of proton-transfer-reaction mass spectrometry (PTR-MS) — Medical applications, food control and environmental research. *Int. J. Mass Spectrom.* **173,** 191–241 (1998).
40. Gautrois, M. & Koppmann, R. Diffusion technique for the production of gas standards for atmospheric measurements. *J. Chromatogr. A* **848,** 239–249 (1999).
41. DeCarlo, P. F. *et al.* Field-deployable, high-resolution, time-of-flight aerosol mass spectrometer. *Anal. Chem.* **78,** 8281–8289 (2006).
42. Jayne, J. T. *et al.* Development of an aerosol mass spectrometer for size and composition analysis of submicron particles. *Aerosol Sci. Technol.* **33,** 49–70 (2000).
43. Vanhanen, J. *et al.* Particle size magnifier for nano-CN detection. *Aerosol Sci. Technol.* **45,** 533–542 (2011).
44. Kangasluoma, J. *et al.* Remarks on ion generation for CPC detection efficiency studies in sub-3-nm size range. *Aerosol Sci. Technol.* **47,** 556–563 (2013).
45. Ehn, M. *et al.* An instrumental comparison of mobility and mass measurements of atmospheric small ions. *Aerosol Sci. Technol.* **45,** 522–532 (2011).
46. Zhao, J., Ortega, J., Chen, M., McMurry, P. H. & Smith, J. N. Dependence of particle nucleation and growth on high-molecular-weight gas-phase products during ozonolysis of alpha-pinene. *Atmos. Chem. Phys.* **13,** 7631–7644 (2013).
47. Mauldin, R. L., Tanner, D. J., Heath, J. A., Huebert, B. J. & Eisele, F. L. Observations of H_2SO_4 and MSA during PEM-Tropics-A. *J. Geophys. Res.* **104,** 5801–5816 (1999).
48. Viggiano, A. A., Seeley, J. V., Mundis, P. L., Williamson, J. S. & Morris, R. A. Rate constants for the reactions of $XO_3^-(H_2O)_n$ (X = C, HC, and N) and $NO_3^-(HNO_3)n$ with H_2SO_4: implications for atmospheric detection of H_2SO_4. *J. Phys. Chem. A* **101,** 8275–8278 (1997).
49. Su, T. & Bowers, M. T. Ion-polar molecule collisions — effect of molecular size on ion-polar molecule rate constants. *J. Am. Chem. Soc.* **95,** 7609–7610 (1973).
50. Hildebrandt, L., Donahue, N. M. & Pandis, S. N. High formation of secondary organic aerosol from the photo-oxidation of toluene. *Atmos. Chem. Phys.* **9,** 2973–2986 (2009).
51. Matsunaga, A. & Ziemann, P. J. Gas-wall partitioning of organic compounds in a Teflon film chamber and potential effects on reaction product and aerosol yield measurements. *Aerosol Sci. Technol.* **44,** 881–892 (2010).
52. Kokkola, H. *et al.* The role of low volatile organics on secondary organic aerosol formation. *Atmos. Chem. Phys. Discuss.* **13,** 14613–14635 (2013).
53. Nieminen, T., Lehtinen, K. E. J. & Kulmala, M. Sub-10 nm particle growth by vapor condensation — effects of vapor molecule size and particle thermal speed. *Atmos. Chem. Phys.* **10,** 9773–9779 (2010).
54. Peeters, J., Nguyen, T. L. & Vereecken, L. HO*x* radical regeneration in the oxidation of isoprene. *Phys. Chem. Chem. Phys.* **11,** 5935–5939 (2009).
55. Silva, G., Graham, C. & Wang, Z. F. Unimolecular β-hydroxyperoxy radical decomposition with OH recycling in the photochemical oxidation of isoprene. *Environ. Sci. Technol.* **44,** 250–256 (2010).
56. Crounse, J. D., Paulot, F., Kjaergaard, H. G. & Wennberg, P. O. Peroxy radical isomerization in the oxidation of isoprene. *Phys. Chem. Chem. Phys.* **13,** 13607–13613 (2011).
57. Kuwata, K. T., Dibble, T. S., Sliz, E. & Petersen, E. B. Computational studies of intramolecular hydrogen atom transfers in the β-hydroxyethylperoxy and β-hydroxyethoxy radicals. *J. Phys. Chem. A* **111,** 5032–5042 (2007).
58. Vereecken, L., Nguyen, T. L., Hermans, I. & Peeters, J. Computational study of the stability of α-hydroperoxyl-α-alkylperoxyl substituted alkyl radicals. *Chem. Phys. Lett.* **393,** 432–436 (2004).
59. Crounse, J. D. *et al.* Atmospheric fate of methacrolein. 1. Peroxy radical isomerization following addition of OH and O_2. *J. Phys. Chem. A* **116,** 5756–5762 (2012).
60. Ziemann, P. J. Evidence for low-volatility diacyl peroxides as a nucleating agent and major component of aerosol formed from reactions of O_3 with cyclohexene and homologous compounds. *J. Phys. Chem. A* **106,** 4390–4402 (2002).
61. Kwan, A. J. *et al.* Peroxy radical chemistry and OH radical production during the NO_3-initiated oxidation of isoprene. *Atmos. Chem. Phys.* **12,** 7499–7515 (2012).
62. Peeters, J. & Nguyen, T. L. Unusually fast 1,6-H shifts of enolic hydrogens in peroxy radicals: formation of the first-generation C_2 and C_3 carbonyls in the oxidation of isoprene. *J. Phys. Chem. A* **116,** 6134–6141 (2012).
63. Vereecken, L. & Peeters, J. A structure-activity relationship for the rate coefficient of H-migration in substituted alkoxy radicals. *Phys. Chem. Chem. Phys.* **12,** 12608–12620 (2010).
64. Méreau, R., Rayez, M. T., Rayez, J. C., Caralp, F. & Lesclaux, R. Theoretical study on the atmospheric fate of carbonyl radicals: kinetics of decomposition reactions. *Phys. Chem. Chem. Phys.* **3,** 4712–4717 (2001).
65. Atkinson, R. *et al.* Evaluated kinetic, photochemical and heterogeneous data for atmospheric chemistry. 5. IUPAC subcommittee on gas kinetic data evaluation for atmospheric chemistry. *J. Phys. Chem. Ref. Data* **26,** 521–1011 (1997).
66. Tobias, H. J. & Ziemann, P. J. Kinetics of the gas-phase reactions of alcohols, aldehydes, carboxylic acids, and water with the C_{13} stabilized Criegee intermediate formed from ozonolysis of 1-tetradecene. *J. Phys. Chem. A* **105,** 6129–6135 (2001).
67. Jang, M. S., Czoschke, N. M., Lee, S. & Kamens, R. M. Heterogeneous atmospheric aerosol production by acid-catalyzed particle-phase reactions. *Science* **298,** 814–817 (2002).
68. Wang, L. *et al.* Atmospheric nanoparticles formed from heterogeneous reactions of organics. *Nature Geosci.* **3,** 238–242 (2010).
69. Kalberer, M. *et al.* Identification of polymers as major components of atmospheric organic aerosols. *Science* **303,** 1659–1662 (2004).
70. Johnson, D. & Marston, G. The gas-phase ozonolysis of unsaturated volatile organic compounds in the troposphere. *Chem. Soc. Rev.* **37,** 699–716 (2008).
71. Vereecken, L. & Francisco, J. S. Theoretical studies of atmospheric reaction mechanisms in the troposphere. *Chem. Soc. Rev.* **41,** 6259–6293 (2012).
72. Saunders, S. M., Jenkin, M. E., Derwent, R. G. & Pilling, M. J. Protocol for the development of the Master Chemical Mechanism, MCM v3 (Part A): tropospheric degradation of non-aromatic volatile organic compounds. *Atmos. Chem. Phys.* **3,** 161–180 (2003).
73. Jenkin, M. E., Saunders, S. M., Derwent, R. G. & Pilling, M. J. Construction and application of a master chemical mechanism (MCM) for modelling tropospheric chemistry. *Abstr. Pap. Am. Chem. Soc.* **214,** 116-COLL (1997).
74. Mauldin, R. L. *et al.* A new atmospherically relevant oxidant of sulphur dioxide. *Nature* **488,** 193–196 (2012).
75. Sharma, S., Raman, S. & Green, W. H. Intramolecular hydrogen migration in alkylperoxy and hydroperoxyalkylperoxy radicals: accurate treatment of hindered rotors. *J. Phys. Chem. A* **114,** 5689–5701 (2010).
76. Raatikainen, T. *et al.* Physicochemical properties and origin of organic groups detected in boreal forest using an aerosol mass spectrometer. *Atmos. Chem. Phys.* **10,** 2063–2077 (2010).

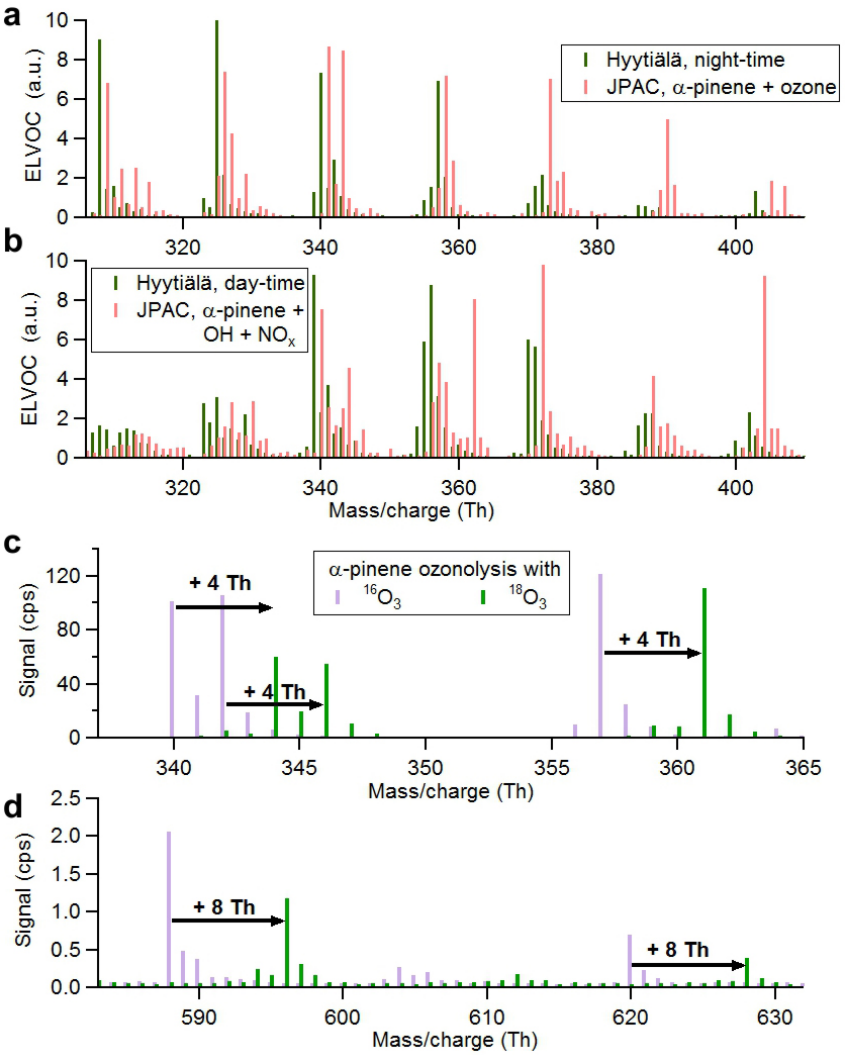

Extended Data Figure 1 | Comparisons of ELVOC spectra. **a**, **b**, Comparison of CI-APi-TOF spectra from Hyytiälä and JPAC, during night (**a**) and day (**b**). The JPAC spectra (light red) show ELVOCs clustered with $^{15}NO_3^-$ whereas Hyytiälä data are clustered with $^{14}NO_3^-$, and therefore identical ELVOCs will be found shifted by 1 Th. The features of the night-time spectrum measured in Hyytiälä are very similar to those in the JPAC α-pinene ozonolysis (2 p.p.b. α-pinene, 17 p.p.b. ozone) spectrum (**a**), with the same pattern of peaks, as well as most major single peaks in good agreement. The day-time Hyytiälä ELVOC spectrum is also replicated quite well, but here using conditions where α-pinene is mainly oxidized by OH, in the presence of NO_x (0.7 p.p.b. α-pinene, 20 p.p.b. ozone, 10^7 cm^{-3} OH, 30 p.p.b. NO_x, ~3 p.p.b. NO). The patterns overlap, and although some single peaks are only found in one of the spectra, the major peaks such as the organic nitrates at 339 Th and 371 Th ($C_{10}H_{15}NO_9$ and $C_{10}H_{15}NO_{11}$) in the Hyytiälä spectrum are found at 340 Th and 372 Th in the JPAC spectrum, as expected. The fraction of α-pinene reacting with ozone in **b** is probably higher in Hyytiälä than under our chamber conditions. The use of labelled nitrate enables us to assign the N-atom to the ELVOCs and not to clustered HNO_3. The peak at 402 Th in the Hyytiälä spectrum in **b**, on the other hand, corresponds to the same ELVOC as 339 Th, with one additional HNO_3 adduct. The corresponding peak in the JPAC spectrum is now shifted to 404 Th, due to the presence of two ^{15}N-atoms. **c**, **d**, ELVOC peak shifts due to isotopically labelled ozone during α-pinene ozonolysis measurements in the Tropos flow tube at 25% relative humidity, using 80 p.p.b. α-pinene. Ozone concentrations, both labelled and non-labelled, were roughly 15 p.p.b. c.p.s., counts per second.

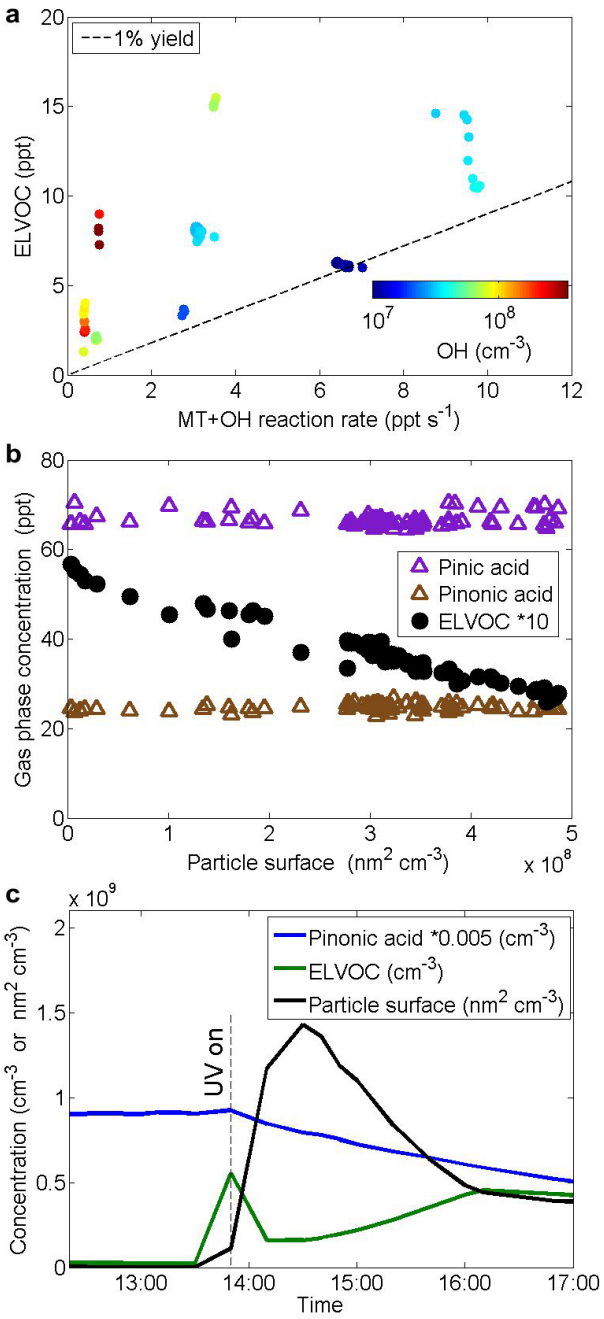

Extended Data Figure 2 | OH oxidation experiments. **a**, Formation of ELVOCs by hydroxyl radical (OH) oxidation of α-pinene. As in Fig. 2a, the yield is estimated on the basis of the amount of monoterpene (MT) reacted. The α-pinene reactions with ozone and the ELVOCs produced from ozonolysis have been accounted for, and they were always <40% of the total ELVOCs and <10% of the reacting MT. At higher OH concentrations, the apparent yield increases, suggesting that multiple OH oxidation steps may produce ELVOCs. At the lowest OH concentrations used (dark blue data points), the ELVOC yield is about 1%, and we take this as an upper limit for the prompt formation of ELVOCs by OH oxidation of α-pinene. If the influence of ozone was not accounted for, the maximum OH yield estimate would still be <1.5%. Therefore, the OH formed during ozonolysis, when the O_3/OH ratio was 10–1,000 times higher than in the experiments depicted here (5–45 p.p.b. ozone, 8×10^6 to 4×10^8 cm^{-3} OH, 0.1–17 p.p.b. α-pinene), will only make a minor contribution to ELVOC formation. This was further supported by only a minor effect on ELVOCs observed when 30 p.p.m. CO was added to scavenge OH in the chamber during ozonolysis experiments. **b**, Gas phase oxidation products versus particle surface area during OH oxidation of α-pinene (0.7 p.p.b. α-pinene, 53 p.p.b. ozone, 10^8 cm^{-3} OH). The amount of ammonium sulphate seed aerosol in the chamber was varied, and ELVOCs decreased as the particle surface area (that is, condensation sink) increased. At the same time, the gas phase concentrations of semi-volatile oxidation products like pinic and pinonic acid measured by the UW HR-ToF-CIMS remained largely unperturbed. This is further supported by the filter sampling, which showed that the SOA explained by pinic acid always remained <3%. The fraction of these vapours entering the particle phase is thus either very small, or the equilibration process extremely slow (on the order of hours), and as we see a clear decrease in ELVOCs, and this loss explains the majority of the measured SOA, the observed SVOC behaviour is consistent with our other findings. During the ozonolysis seed addition experiments reported in Fig. 2, the UW HR-ToF-CIMS was focused on measuring particle phase composition with the filters, and therefore reliable data for the SVOCs can only be presented for OH oxidation experiments. However, the condensation dynamics are not expected to change considerably between the two cases. **c**, Formation of ELVOCs from pinonic acid oxidation by hydroxyl radicals (OH). Pinonic acid was added to the chamber and once stable (at 13:50), the ultraviolet lights were turned on and ELVOC concentrations increased rapidly, in accordance with prompt formation of ELVOCs from the pinonic acid + OH reactions. The ELVOCs quickly decrease after this, due to a large condensation sink produced by the formed aerosol particles. The ELVOCs increase again as the amount of aerosol surface decreases, in line with the expected ELVOC behaviour. The starting ozone concentration was 80 p.p.b., and this concentration dropped to 40 p.p.b. after the ultraviolet light was turned on. Once the light had been turned on, the resulting OH concentrations were estimated to be 2×10^8 cm^{-3}. The apparent increase before ultraviolet lights were turned on is due to the low time resolution of the data. All concentrations stayed stable until the ultraviolet lights were turned on.

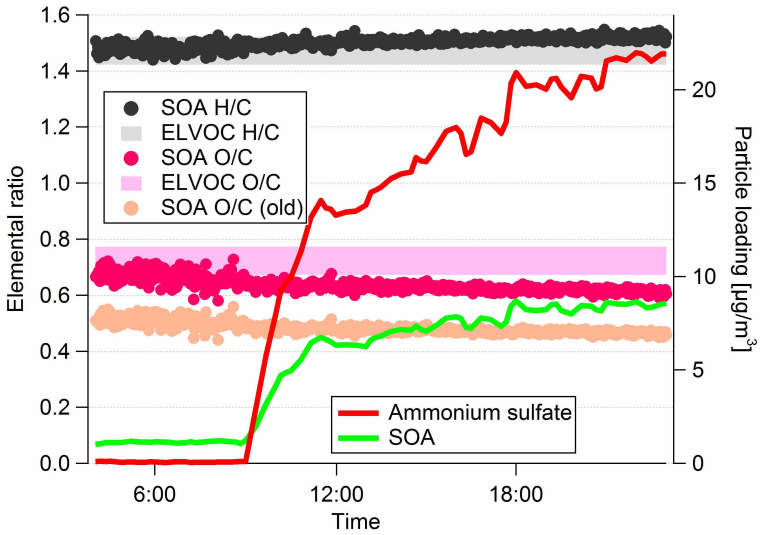

Extended Data Figure 3 | Elemental ratios measured by the AMS during ammonium sulphate seed addition. The period corresponds to that shown in Fig. 2b. At 09:00 ammonium sulphate was added, and there is a slight decrease in the O/C ratio, consistent with more SVOCs being able to condense at higher SOA loading. Before the seed addition, the data are noisier owing to the relatively low SOA loading, but during this period we expect only ELVOCs to be able to condense onto the particles. The calculated O/C and H/C ratios for the gas phase ELVOCs are shown in shaded pink and grey, respectively. Again, at higher loadings the values start to diverge, consistent with an increased contribution from SVOCs to SOA mass. The O/C and H/C were calculated according to an improved elemental analysis methodology (M.C. *et al.*, manuscript in preparation). The light orange dots depict the SOA O/C calculated using the old methodology commonly used until now, yielding values that are lower by roughly 0.15–0.2. These values are consistent with previous α-pinene ozonolysis experiments[16] as well as average O/C values measured in Hyytiälä[76]. It should, however, be noted that the ability of the AMS to provide accurate O/C is dependent on the specific compounds, and together with possible particle-phase evolution, the gas and particle phase O/C is not expected to match perfectly even if completely error-free measurements were possible.

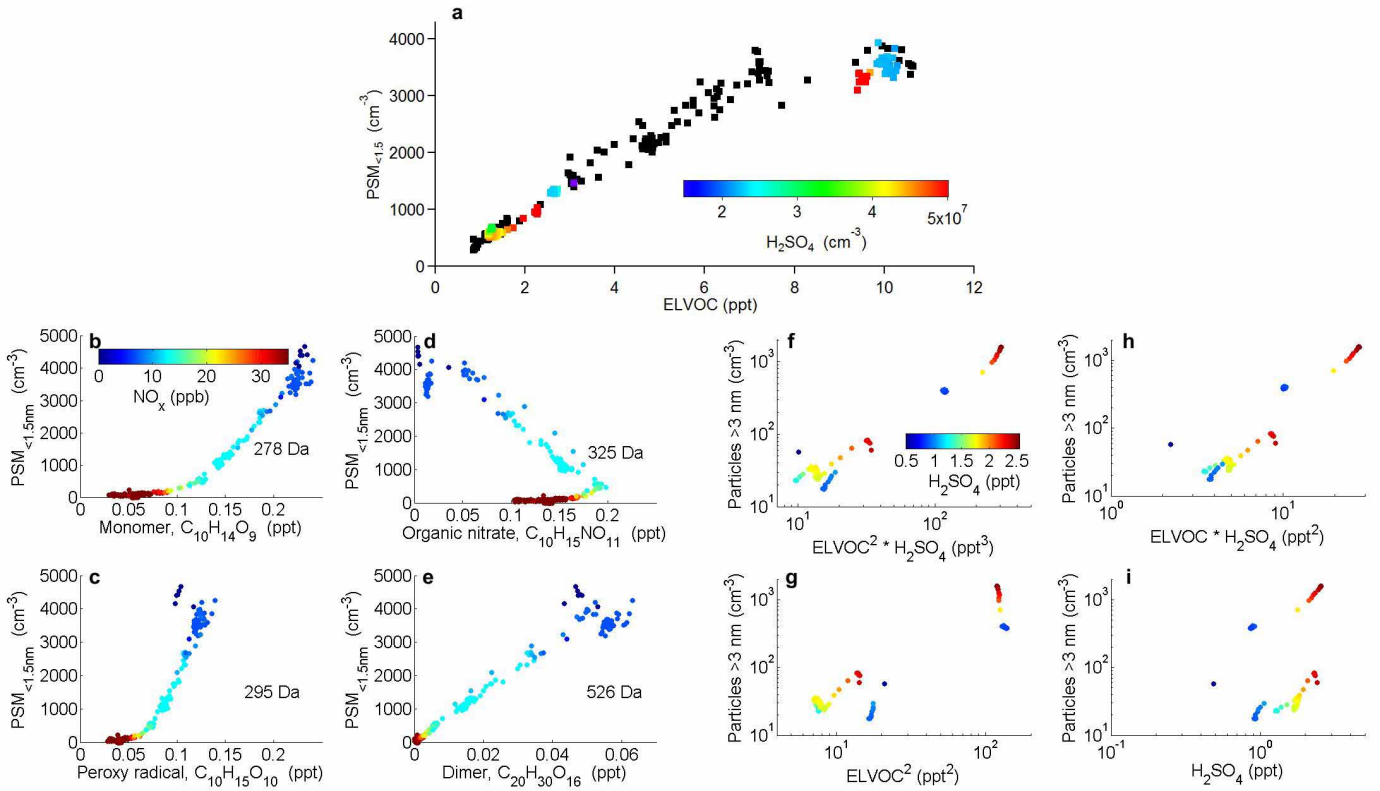

Extended Data Figure 4 | Nano-CN and particle dependence on ELVOCs. **a**, The concentration of particles smaller than ~1.5 nm in diameter, as measured by the particle size magnifier, PSM ($PSM_{<1.5nm}$), correlates extremely well with ELVOC concentrations. The black squares correspond to the same period as plotted in Fig. 2a; coloured squares were measured during SO_2 addition and correspond to the same period as in Fig. 2d. These data show that $PSM_{<1.5nm}$ is independent of H_2SO_4, in line with the PSM directly detecting some fraction of the ELVOCs. The slope of the relationship is consistent with reported $PSM_{<1.5nm}$ detection efficiencies of <1% for organic ions of this size[44]. The linear correlation, which is independent of H_2SO_4 concentrations, links the large ELVOC molecules formed by α-pinene oxidation and measured by mass spectrometric methods to nano-CN[24]. During these experiments, ELVOC monomers and dimers showed a clear correlation, and therefore no conclusions could be drawn about which ELVOCs were actually detected by the PSM. **b**–**e**, $PSM_{<1.5nm}$ dependence on different ELVOCs during NO_x additions. The data correspond to the same time period as in Extended Data Fig. 10b. We find that monomers (**b**), peroxy radicals (**c**) and organic nitrates (**d**), all with masses around 300 Da, are still found in the chamber after $PSM_{<1.5nm}$ has reached zero. However, the dimers, that is, the largest ELVOCs observed, with masses around 500 Da, show a linear dependence with $PSM_{<1.5nm}$ (**e**), indicating that ELVOC dimers can act as nano-CN. This suggests that dimers may also act as condensation nuclei for vapours in the atmosphere under certain conditions. **f**–**i**, Particles larger than 3 nm as a function of different combinations of ELVOC and H_2SO_4 concentrations. Panel **f** shows the combination plotted in Fig. 2d, which gives a near-linear dependence. Also [ELVOC] × [H_2SO_4] gives a relatively linear slope (**h**), though low-H_2SO_4 points become more offset. The agreement becomes much worse when neglecting either compound completely (**g**, **i**). Bases such as ammonia and amines may influence the particle formation in addition to H_2SO_4 and ELVOCs, but any background levels of these compounds in JPAC probably stayed constant enough during these experiments to not influence the observed slopes.

a

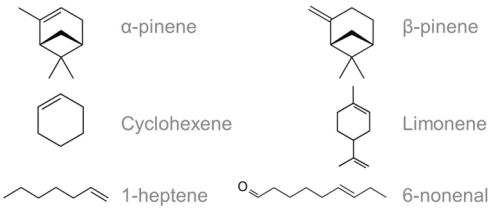

b

VOC	ELVOC molar yield
Cyclohexene	4%
α-pinene	7%
Limonene	17%
ß-pinene	<0.1%

Extended Data Figure 5 | Structures and ELVOC yields of different VOCs. **a**, Structures of the main compounds studied in this work. **b**, ELVOC molar yields of selected VOCs during ozonolysis. The reported yields are subject to the absolute ELVOC concentration uncertainty (±50%), but the relative concentrations are more precise. No OH scavenger was used during these experiments.

a

	Range, unitless	Relative uncertainty (δ)
Collision frequency (CF)	0.85±0.15 (0.7-1.0)	0.18
Transmission efficiency (TE)	1.5±0.5 (1-2)	0.33
Inlet wall losses (WL)	60±15 (45-75)	0.25
Residence time (RT)	200±50 (150-250)	0.25

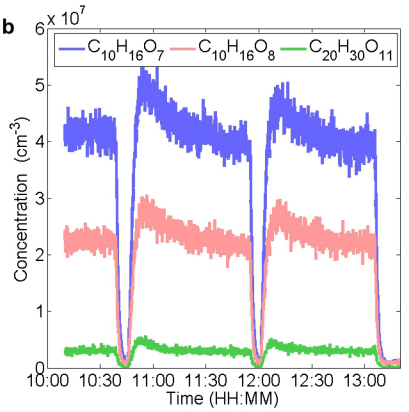

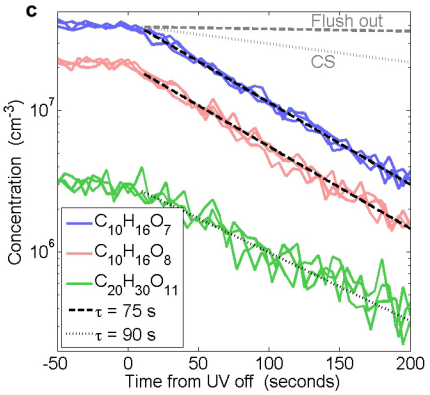

d

	α-pinene	Ozone	Other notes
Figure 1	6.4 ppb	78 ppb	
Figure 2A	0-30 ppb	12-86 ppb	
Figure 2B & 2C	19 ppb	83 ppb	Chamber input had 34 ppb α-pinene, of which ~9 ppb reacted with ozone and ~6 ppb with OH
Figure 2D	0.5-6.5 ppb	87-90 ppb	$[SO_2]$ = 3-45 ppb

Extended Data Figure 6 | Instrumental and chamber details influencing ELVOC yield calculations. **a**, Estimated uncertainty sources, and corresponding ranges, in the quantification of ELVOCs using the CI-APi-TOF. The transmission efficiency (TE) of ions in the CI-APi-TOF can vary depending on the ions' mass/charge. If the transmission in the mass range where ELVOCs are measured (300–700 Th) is different from that for the nitrate ions (62–188 Th) used for normalizing, the ratio *A* (see Methods section 'ELVOC detection and quantification using the CI-APi-TOF') will be influenced. We estimate a maximum influence of a factor of 2 from this source. The nominal residence time for ion–molecule collisions in the charger is 200 ms, but if the mixing of ions into the sample flow is not instantaneous, or either the sample or sheath flows are offset, the residence time will change. We estimate a maximum error in the residence time of 50 ms. **b**, Time series of three OH-produced ELVOC molecules during switching of ultraviolet lights on and off in JPAC. When the ultraviolet lights were turned off, the OH concentration quickly dropped, and we consequently observed the decay of OH-produced ELVOCs. Once sufficient decay had been observed, the ultraviolet lights were turned back on, and both OH and the plotted ELVOCs quickly increased to their original levels. This experiment was repeated three times. **c**, The concentrations are plotted relative to the time when the ultraviolet was switched off. The exponential ELVOC decay corresponded to lifetimes (τ) of 75–90 s. The much longer decay times corresponding to ELVOC losses to particles (condensation sink, CS, grey dotted line) and flush out (grey dashed line) are also plotted. **d**, Steady-state chamber conditions during experiments presented in Figs 1 and 2. See Methods for details of parameters that were kept constant.

a

1. MT + O_3 → λ · OVOC + γ_{RO2} · RO_2 + (1 - λ - γ_{RO2}) · $R'O_2$ + OH + 0.001 · HO_2	$k_{a\text{-pinene + O3}}$
2a. $R'O_2$ → α · $R''O_2$ + (1-α) · Products	$k_{H\text{-shift/O2-addition}}$
2b. $R''O_2$ → α · $R'''O_2$ + (1-α) · Products	$k_{H\text{-shift/O2-addition}}$
2c. $R'''O_2$ → α · $R_{ELVOC}O_2$ + (1-α) · Products	$k_{H\text{-shift/O2-addition}}$
2d. $R_{ELVOC}O_2$ → Products	$k_{H\text{-shift/O2-addition}}$
3a. ΣRO_2 + RO_2 (or HO_2) → Products	$k_{RO2+RO2}$ (or $k_{RO2+HO2}$)
3b. ΣRO_2 + NO → Products + HO_2	$k_{RO2 + NO}$
4a. $R_{ELVOC}O_2$ + RO_2 (or HO_2) → β · $ELVOC_{Monomer}$ + (1-β) · $ELVOC_{Dimer}$	$k_{RELVOCO2 + RO2}$
4b. $R_{ELVOC}O_2$ + NO → χ · $ELVOC_{Nitrate}$ + (1-χ-ϕ) · [Products + HO_2] + ϕ · $ELVOC_{monomer}$	$k_{RO2 + NO}$
5a. ΣRO_2 + wall →	$k_{wall\ loss}$
5b. $R_{ELVOC}O_2$ + wall →	$k_{wall\ loss}$
5c. ELVOC + wall→	$k_{wall\ loss}$

b

Parameter	$Value_A$	$Value_B$
α-pinene	0-11 ppb	5 ppb
NO	0 ppb	0.3-5 ppb
Ozone	80 ppb	
k (α-pinene + O_3)*	$8.4 \cdot 10^{-17}$ cm^3 s^{-1}	
k (H-shift)	0.5 s^{-1}	
k ($R_{ELVOC}O_2$ + RO_2)†	$5.0 \cdot 10^{-11}$ cm^3 s^{-1}	
k (RO_2 + RO_2)	$1.0 \cdot 10^{-12}$ cm^3 s^{-1}	
k (RO_2 + HO_2)*	$2.7 \cdot 10^{-11}$ cm^3 s^{-1}	
k (RO_2 + NO)‡	$4.7 \cdot 10^{-12}$ cm^3 s^{-1}	
k (wall loss)	0.011 s^{-1}	
Temperature	288 K	
Pressure	1 atm	
Relative humidity	65 %	

Extended Data Figure 7 | Kinetic box model details. **a**, The key reactions used to model the ELVOC system, with species coloured according to Extended Data Fig. 10. ∑RO_2 indicates all non-ELVOC peroxy radical species (RO_2, $R'O_2$, $R''O_2$ and $R'''O_2$). **b**, Parameters used in the kinetic model for runs A and B, corresponding to results in Extended Data Fig. 10d and e, respectively. *Suggested by MCM; †for simplicity, OH reactions were excluded from the model, and although these do not produce a significant fraction of ELVOCs, their contribution to RO_2 is non-negligible. Thus, our model will underpredict RO_2, which is partly compensated by a relatively high $R_{ELVOC}O_2$ + RO_2 rate coefficient; ‡Half that suggested by MCM.

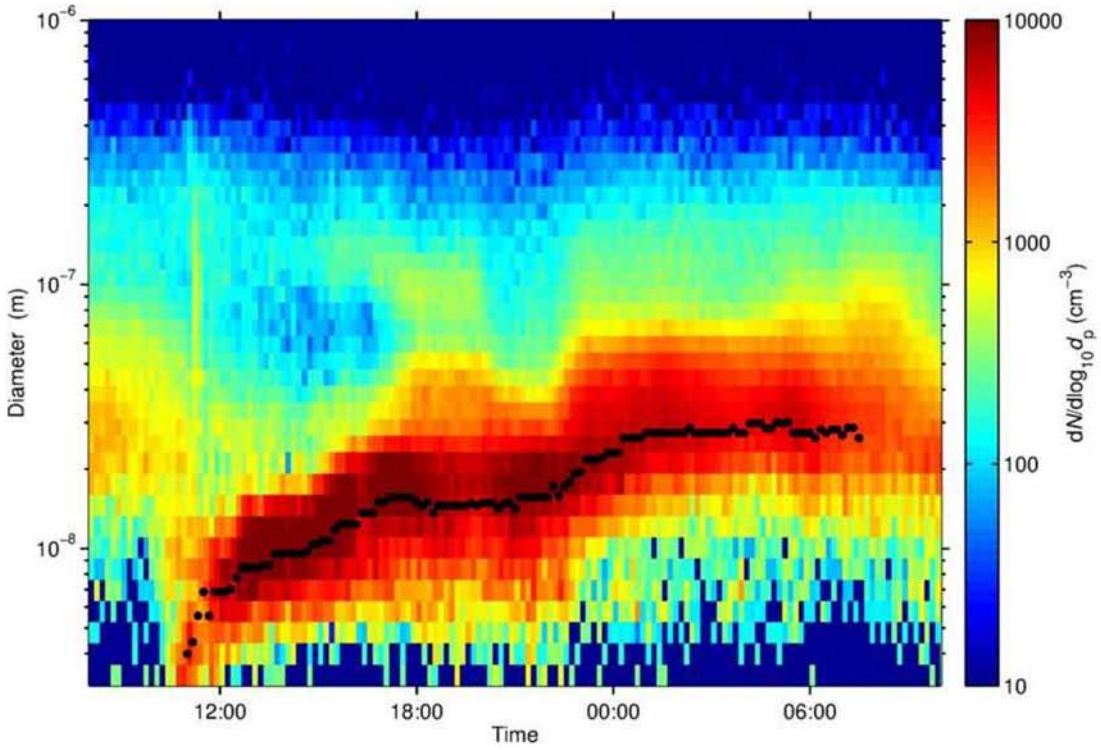

Extended Data Figure 8 | Particle formation and growth event on 26–27 March 2011 in Hyytiälä. The colour-coded data in this figure depict the aerosol particle concentration as a function of particle diameter and time. A high concentration, as signified by the dark red colour, of small particles appears around noon on 26 March, and this particle mode grows throughout the night. The nucleation mode geometric mean diameters obtained by log-normal fits are shown by black dots.

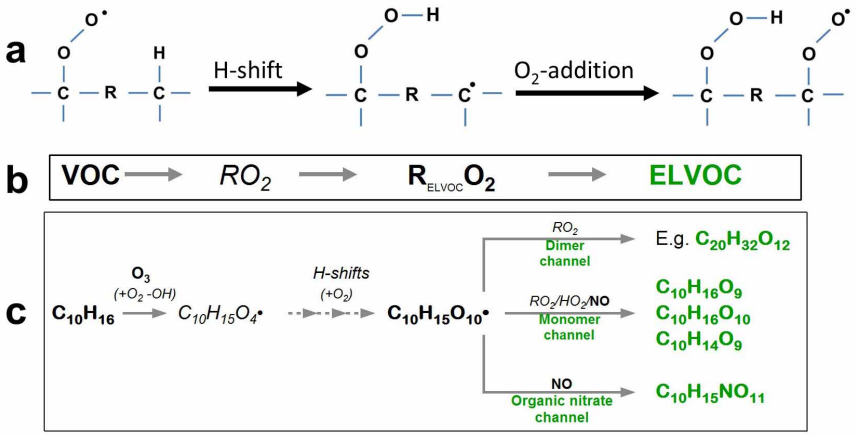

Extended Data Figure 9 | Schematic illustrations of ELVOC formation. **a**, Internal hydrogen abstraction by an RO_2 ('H-shift'), followed by oxygen addition at the alkyl radical site, forming a more oxidized peroxy radical. Depending on the exact structure of the molecule, this new RO_2 can perform subsequent H-shifts/O_2-additions to increase the oxygen content even further. **b**, **c**, Simplified diagram of ELVOC formation. The general form is shown in **b**, and a specific example pathway from α-pinene ($C_{10}H_{16}$) ozonolysis in **c**. For clarity, all reactions not leading to ELVOCs are omitted. The first reaction yields a peroxy radical (**b**: RO_2, **c**: $C_{10}H_{15}O_4^{\bullet}$), that can undergo several fast H-shift reactions followed by O_2-addition, resulting in more oxidized peroxy radicals (**b**: $R_{ELVOC}O_2$, **c**: $C_{10}H_{15}O_{10}^{\bullet}$). $R_{ELVOC}O_2$ can react through well-established pathways with either HO_2, RO_2 or NO, all of which can form ELVOCs. The relative abundance of these species as well as the rates of the unimolecular decomposition reactions determines the overall ELVOC mass yield, while not necessarily affecting the molar yield. Only reactions of $R_{ELVOC}O_2$ with other RO_2 can form dimers ($R_{ELVOC}OOR$), whereas organic nitrates ($R_{ELVOC}ONO_2$) only form in reactions with NO. All compounds in bold font were directly measured.

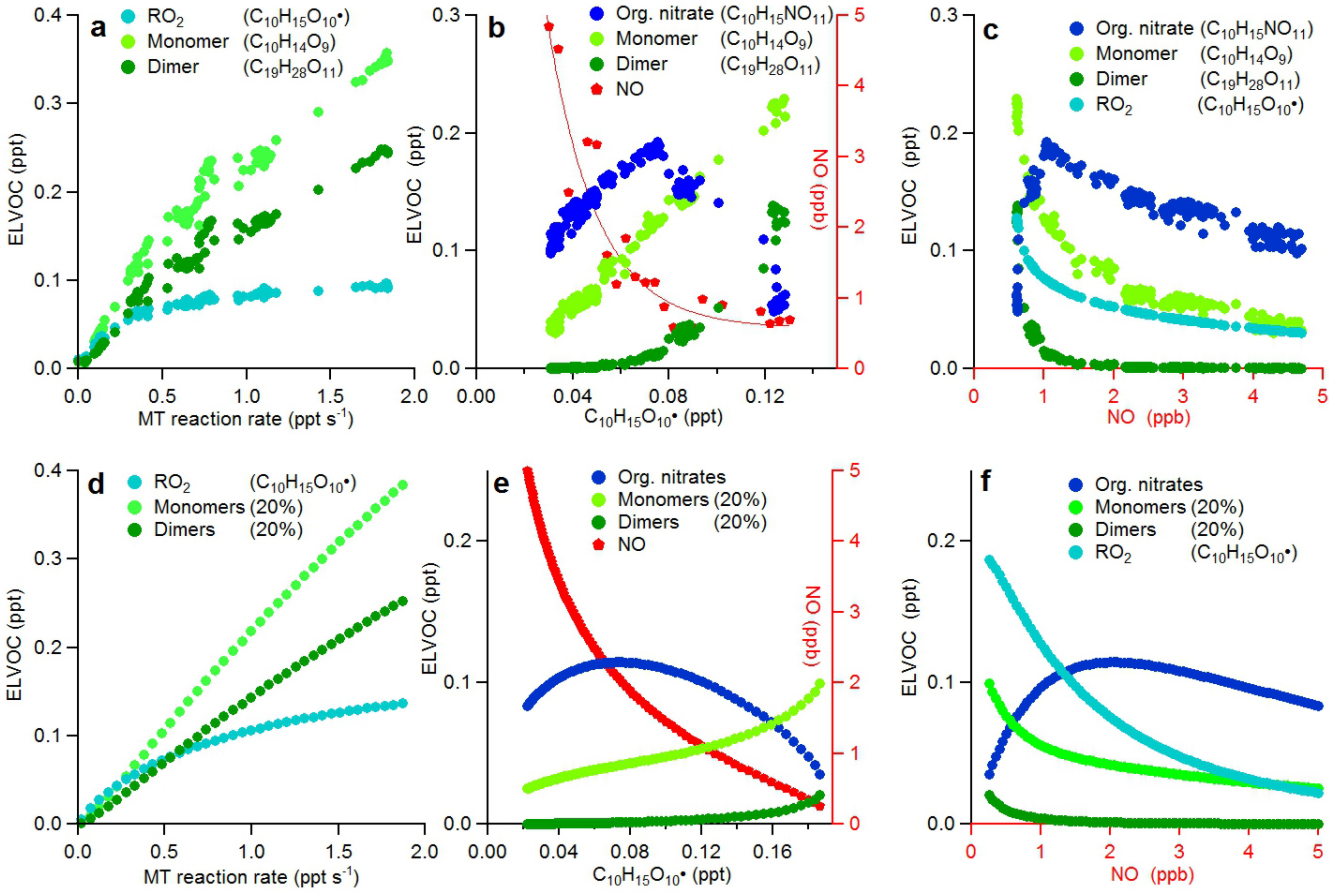

Extended Data Figure 10 | Responses of ELVOC sub-groups to varying chamber conditions. **a**–**c**, Measured ELVOC behaviour during low-NO_x (**a**) and high-NO_x (**b**, **c**) experiments. Data in **a** are from the same experiments as shown in Fig. 2a, conditions in **b** varied within the following ranges: 0–70 p.p.b. NO_x, 80–90 p.p.b. ozone, 6–7 p.p.b. α-pinene. The RO_2 radicals increase roughly as the square root of the α-pinene reaction rate, whereas the closed shell molecules show a more linear dependence, as expected. In **b**, α-pinene and ozone are kept constant, while adding different amounts of NO_x. Panel **c** contains the same data as **b**, but with the data plotted against the fitted NO concentration acquired from **b**. **d**–**f**, Modelled ELVOC behaviour during low-NO_x (**d**) and high-NO_x (**e**, **f**) conditions, simulating the experiments plotted in **a**–**c**. For the monomers and dimers, one-fifth (20%) of the total products is plotted, for a better comparison with **a**–**c**, where only specific molecules are shown.